Parametric effects on the flow redistribution in ballooned bundles evaluated by magnetic resonance velocimetry

A.V.S. Oliveira, Didier Stemmelen, S. Leclerc, T. Glantz, Alexandre Labergue, G. Repetto, Michel Gradeck

Parametric effects on the flow redistribution in ballooned bundles evaluated by magnetic resonance velocimetry

A. V. S. Oliveira[a,b], D. Stemmelen[b], S. Leclerc[b], T. Glantz[a], A. Labergue[b], G. Repetto[a], M. Gradeck[b,*]

[a] *IRSN, PSN, B.P. 3, 13115 Saint Paul-Lez-Durance, France*
[b] *Université de Lorraine, CNRS, LEMTA, F-54000 Nancy, France*

Abstract

When the water inventory evaporates during a hypothetical loss of coolant accident in the core of a pressurized water reactor, the fuel rods temperature increases substantially, resulting in the clad ballooning and the formation of blocked sub-channels. During the reflooding phase, where water is injected into the core and a steam-droplets flow is created above the water level, the presence of ballooned zone forces the steam flow to redistribute towards intact sub-channels, which degrades the cooling of ballooned clads within blocked sub-channels. Looking to better understand this flow redistribution process, this study presents experimental results of magnetic resonance velocimetry measurements of three-component velocity fields in several 49-element ballooned bundles to evaluate geometric effects (blockage ratio, length and coplanarity) on the flow dynamics, as well as the flow rate effect (Reynolds number from 1,936 to 9,599). The flow redistribution occurred in the transition zone upstream of the balloon. Moreover, the transverse velocities at this location are higher for higher blockage ratios and they can reach nearly the same magnitude of the axial velocity. The amount of deviated flow is approximately equal to the sub-channel's blockage ratio and is virtually insensitive to the blockage length or the flow rate. Furthermore, the flow axial velocity reduces up- and downstream of blocked sub-channels and this reduction is more substantial as the blockage ratio increases. Results with non-coplanar balloons showed that a less intense flow redistribution takes place; however, a downstream balloon can affect the flow redistribution dynamics caused by an upstream ballooned zone. Finally, for all the tested bundles and tested flow rate ranges, the flow was remarkably homogenized by the downstream mixing spacer grid, restricting the clad ballooning effects only to the portion between the two spacer grids were the ballooned zone is located regardless of the balloon geometry and the flow rate. The present results may be useful as well for other research areas involving flow blockages in heat exchangers.

Keywords:
Magnetic resonance imaging, LOCA, Nuclear reactor, Blockage, Thermal-hydraulics, Fluid dynamics

1. Introduction

Loss of coolant accident, usually referred as LOCA, is a hypothetical accidental condition in which there is a leak in the primary circuit of a pressurized water reactor (PWR) and, consequently, the water inventory may evaporate, leading to the degradation of the heat dissipation from the fuel rods. Hence, their temperature increases significantly and, because of the internal pressure within the fuel rods, the clads may swell or even burst, as shown in Fig. 1 [1].

*Corresponding author
Email address: michel.gradeck@univ-lorraine.fr (M. Gradeck)

To avoid occurring a severe accident, emergency core cooling systems (ECCS) are activated and it injects water into the nuclear reactor's core to immerse and cool the fuel assemblies. As the water level rises, a dispersed two-phase flow is created with steam generated from evaporated water at the triple interface of solid-liquid-vapor and droplets generated by bursting and spattering at this interface and by shearing between liquid and steam. While we find some studies investigating flow boiling and its fluid dynamics [2–4], which is the predominant heat transfer phenomenon in a LOCA during the pre-dryout condition, this dispersed flow plays a very important role in the cooling of the fuel assemblies' parts that are still not immersed in water. For this reason, several reflooding experiments have been performed in the past [5] but also more recently [6, 7] with the evolution of measurement techniques, especially concerning clad ballooning as we discuss in the next paragraphs.

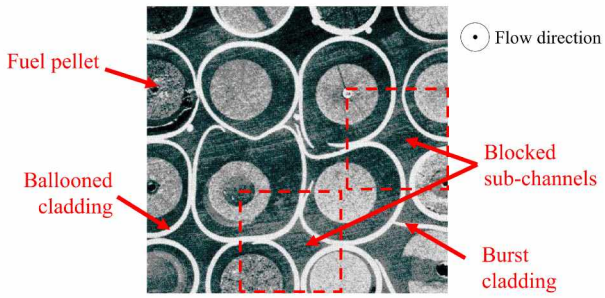

Figure 1: Clad ballooning and appearance of blocked sub-channels after an in-pile LOCA experiment (adapted from [1]).

In the presence of blocked sub-channels, the steam deviates towards intact sub-channels that are less resistant to the flow [8]. As a consequence, the heat dissipation in these blocked sub-channels is highly reduced, especially because wall-to-steam convection is one of the main heat transfer paths for the fuel rods cooling [9, 10]. This motivated several studies in the literature to analyze the effects of clad ballooning and the thermal-hydraulics in blocked sub-channels using fuel rod bundles [11, 12] and at sub-channel scale [13–15]. Grandjean [5] compiled several past experimental campaigns in a state-of-the-art review in 2007 and he observed that many experimental results suggested that clad ballooning might be large and long enough so a blocked sub-channel can no longer be coolable. Also, the cited experiments showed that the region downstream of the balloon might be a critical region as this is one of the most affected parts by the flow redistribution. Particularly, he cited the FLECHT-SEASET reflood experiments in a bundle of 21 elements that occurred in the 1980's [16] using, among other configurations, coplanar and non-coplanar balloons. We define as coplanar balloons the case where the ballooned fuel rods are at the same axial position and they create a single ballooned zone, while non-coplanar balloons is the configuration with ballooned fuel rods located at different axial positions, which consequently can create more than one ballooned zones. For the tested non-coplanar geometries, their results showed that the blockage configuration has little effect on the heat transfer process.

We find other studies concerning the thermal-hydraulics in LOCA conditions with clad ballooning. Kim et al. [11] performed reflooding experiments representing a large-break LOCA in one intact 6x6 fuel rod bundle and two 5x5 ballooned bundles, one without changing the axial heating power profile and the other with higher heating density in the ballooned zone to simulate the fuel relocation effect. They found that the peak cladding temperature (PCT) is virtually the same for the intact and the only-ballooned bundle (with unchanged heating profile), while

it increases for the fuel-relocated bundle. Hong et al. [17] performed experiments representing small and medium-break LOCA conditions in 3x3 intact and ballooned bundles and they observed an increased heat transfer with the ballooned bundle because of increased flow velocity (Venturi effect) and droplets breakup. This phenomenon was also observed by Peña Carrillo et al. [14] in their experimental study at sub-channel scale of the thermal-hydraulics of an internal steam-droplets flow with a constricted tube representing LOCA conditions, which was numerically validated by Oliveira et al. [9] using a mechanistic model. Nevertheless, these results occur due to the absence of flow redistribution, which might not be the case in a real LOCA. Furthermore, flow redistribution strongly affects the thermal-hydraulics in blocked sub-channels where heat dissipation is expected to be much degraded. For instance, Sarkar et al. [18] performed numerical simulations in a bundle of 19 elements to evaluate the effect of porous blockages on the heat dissipation of a fast breeder reactor and they found that the more blocked is the sub-channel the higher the risk of reaching a critical PCT. They correlated the blockage radial extent and porosity to a critical blockage length for which the PCT reaches the sodium boiling point. Moreover, longer blockages have lower coolability, as shown, for example, by Kim et al. [15] in their experimental analysis at sub-channel scale to evaluate the blockage length effect.

Although these and other studies in the literature have evaluated the clad ballooning effect on the thermal-hydraulics during a LOCA in many different ways, experiments measuring precisely three-component velocity fields in ballooned bundles are practically non-existent. One reason for this lack of data is the difficulty to measure accurately the flow in blocked sub-channels. Using physical probes like Pitot tubes would give punctual data and could disturb the flow, and using optical techniques is not easily feasible because there is no optical access. Although significant advance has been obtained using refractive index matching materials [19–21], this technique requires the use of very specific materials and fluids at a controlled temperature to ensure proper measurement conditions. Hence, magnetic resonance velocimetry (MRV) becomes a very interesting technique to provide mean three-component velocity fields. This technique, for example, was used by Piro et al. [22] to measure the flow velocity in a representative CANDU fuel assembly with 37 elements.

MRV was also the technique we used in our previous study [23] to obtain velocity fields of the flow in two 7x7 bundles, one intact and one ballooned, and to observe the flow redistribution process. The ballooned zone consisted of sixteen elements with a blockage ratio of 90% and a blockage length of 240 mm. The blockage ratio τ_b is a common parameter to determine the reduction in the sub-channel cross-sectional area due to clad ballooning and is defined by:

$$\tau_b = 1 - \frac{S_b}{S_0} \tag{1}$$

where S_b and S_0 are, respectively, the cross-sectional area of a blocked and an intact sub-channel. Interesting features of the flow redistribution were found in that study, like: 1) intense transverse velocities were observed upstream of the balloon; 2) there was flow recirculation downstream of the balloon; and 3) the mixing spacer grid downstream of the ballooned zone homogenized the flow. Nevertheless, results with different ballooned zones are necessary to describe precisely the geometric effects on the flow redistribution and then increase our understanding of the LOCA thermal-hydraulics. Thus, the present study provides new experimental results of MRV measurements with several 7x7 ballooned bundles. The geometric effects we analyze herein are the blockage ratio, length and coplanarity (with

coplanar and non-coplanar balloons). Moreover, we evaluated as well the flow rate effect on the flow redistribution.

This study is part of the PERFROI project launched by the French Institut de Radioprotection et de Sûreté Nucléaire (IRSN) to better understand the thermal-mechanics and the thermal-hydraulics phenomena during a LOCA. These MRV experiments will complement the analysis of its main experimental campaign in the thermal-hydraulics axis named COAL[1], which consists of reflooding experiments in a partially ballooned bundle containing 49 elements with electrically-heated fuel rods [24]. Furthermore, the present study provides valuable data for the validation of numerical codes like IRSN's DRACCAR [25, 26] and, more specifically, corroborate its pre-simulations of the COAL experiments [27, 28]. Although we used specific geometries and test conditions for a hypothetical LOCA in a French PWR, the results herein presented provide important insights for any applications with tube bundles, like heat exchangers or fluid mixers. Blockages in these devices due to tube deformation or fouling are not only problematic but also common to take place, and measuring the fluid velocity in these scenarios is also a challenge. Therefore, the MRV technique and test section construction method that we used in this study may also be helpful for those research areas.

2. MASCARA: experimental apparatus and procedure

2.1. Hydraulic circuit

Figure 2 presents the experimental set-up named MASCARA[2], which is basically a conventional hydraulic circuit containing approximately 80 liters of water. This apparatus was specially built for this project and is the same used in our previous study [23] but with new test sections. The schematic drawing only presents the essential components, so some safety solutions like electrovalves and by-passes are hidden to avoid clutter. Ensuring stable fluid flow during the experiment is very important to obtain accurate and stable MRV measurements, thus we used both an eccentric screw pump and a damper for this purpose. An electromagnetic flowmeter was placed in the hydraulic circuit for the later validation of the MRV results by comparing both bulk flow rate values. Moreover, we installed pressure transducers in the line to obtain the system pressure and the pressure drop on the circuit, which served mainly for monitoring and safety purposes.

We performed the experiments using tap water as the test fluid because of its high-intensity signal for the MRV. During a LOCA, the flow actually occurs with steam, but this fluid is unpractical for MRV experiments because of its very low density that provides unreadable signals. Since the flow with water should behave as if it were with steam, we conserved the same Reynolds number based on the hydraulic diameter found during a LOCA (between 1,000 and 10,000). Hence, we tested four different flow rates, whose approximate values are 50, 120, 185 and 245 lpm, with the respective Reynolds number of 1,936, 4,671, 7,223 and 9,599.

2.2. Test sections

We tested six bundles containing forty-nine elements to evaluate the geometry influence on the flow redistribution, more specifically the effects of the blockage ratio τ_b, blockage length L_b and balloons coplanarity. All the tested

[1]COAL: **CO**olability of a fuel **A**ssembly during **L**OCA

[2]MASCARA: **M**RI of **A**ssembly **S**ub-**C**hannels for the **A**nalysis of **R**eactor **A**ccidents

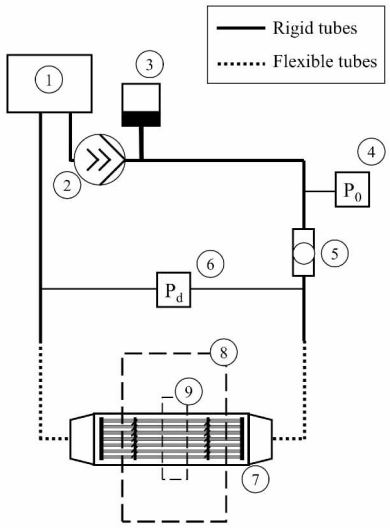

Figure 2: MASCARA experimental set-up: 1) water tank, 2) eccentric screw pump, 3) damper, 4) absolute pressure transducer, 5) electromagnetic flowmeter, 6) differential pressure transducer, 7) test section, 8) MRI scanner, 9) radiofrequency (RF) coil. [23]

bundles, either coplanar and non-coplanar, were designed to be symmetric to an inclined plan (as we present later), which is helpful in future comparisons with numerical simulations as it allows to reduce the calculation domain size and, consequently, its computational cost. Furthermore, they are all structurally similar although they have different ballooned zones. The test section housing is approximately 1.12 m long and the 7x7 bundle is composed of plastic tubes to represent the intact fuel rods and guide tubes and a 3D-printed part to represent the ballooned zone (the base polymer was PLA). We assembled the bundles using four spacer grids. Two of them are bottom and top-end grids (without mixing vanes) mounted at the extremities, while the other two are spacer grids with mixing vanes and they are placed at specific positions along the test section. These spacer grids are actually the same that will be used in COAL experimental campaign, so they are made in Inconel and, consequently, MRV measurements are not feasible near them by 4 cm. Also, two machined aluminum parts were assembled on the extremities of the housing with quick-connectors to attach to the hydraulic circuit's flexible tubes, and capillary plastic tubes were attached to the housing's outer surface to serve as a reference to determine precisely the velocity fields' axial location.

Figure 3 presents the axial position of the spacer grids and the balloon in the coplanar bundles, with their values given in Table 1. We should remark that the distance between the two mixing spacer grids in the middle (E – A) is approximately the same for all the test sections in the present study because this is representative of a French PWR (about 522 mm). Furthermore, the coplanar balloons are placed nearly in the middle between the two mixing spacer grids so we could better analyze the flow behavior up- and downstream.

Figure 4 illustrates the cross-section in an intact zone, with forty-six tubes representing the fuel rods (9.5 mm diameter) and three tubes representing guide tubes (12.45 mm diameter), and the ballooned zone where sixteen fuel rods are shaped according to their respective blockage ratio. The aforementioned test section's symmetry plan, which is a characteristic of all the tested bundles, is represented in the intact zone's cross-section illustration by the inclined dash-dotted line. On the one hand, the ballooned fuel rods with 61% blockage ratio are circular with a diameter that equals the fuel rods pitch (12.6 mm), representing a condition where neighboring clads swell until contacting but

Table 1: Dimensions for coplanar bundles as shown in Fig. 3 (in mm)

Bundle	τ_b	$\mathbf{L}_b$	**A**	**B**	**C**	**D**	**E**	**F**	**E − A**
G61%/100mm	61%	100	252	434	479	625	774	1073	522
G80%/100mm	80%	100	262	428	480	632	784	1079	522
G90%/100mm	90%	100	252	409	474	639	776	1066	524
G90%/240mm	90%	240	282	370	435	740	803	1072	521

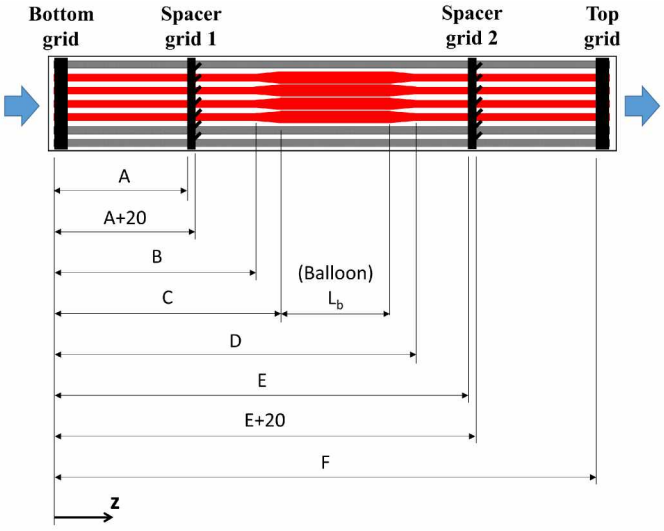

Figure 3: Axial positions of the grids and the balloon in coplanar bundles.

without further deformation. On the other hand, those with 90% and 80% blockage ratios are square with rounded corners, simulating the cladding shape deformation due to continuous swelling even after neighboring clads are in contact (as shown in Fig. 1).

For all the geometries, the transition from the intact to the ballooned zone has the same angle, which means the transition length is different for each bundle. At the beginning of the transition zone, the ballooned fuel rods have their diameter increased until they are in contact but still keeping their circular shape (Fig. 5). At this point, the sub-channel's blockage ratio reaches 61%. However, for higher blockage ratios, there is a second transition zone where the geometry is flattened in the contact with other fuel rods as we presented in Fig. 4. As the transition angle is the same, this transition is longer for higher blockage ratios. In the present study, the first transition zone (where $\tau_b \leq 61\%$) has the same length of 35 mm for all the bundles. However, the second transition zone is 16 mm long for the bundle with 80% blockage ratio and 30 mm long for both bundles with 90% blockage ratio, while it is evidently not existent in the bundle with 61% blockage ratio.

For the non-coplanar bundles, Fig. 6 presents the axial positions for the grids and balloons and the fuel rods arrangement. Their ballooned zones are built with ballooned fuel rods with 80% blockage ratio and blockage length of 100 mm, which is the same used in the G80%/100mm bundle. Moreover, both of them contain four ballooned fuel rods in the first ballooned zone and twelve in the second one but arranged differently. In the first bundle, named

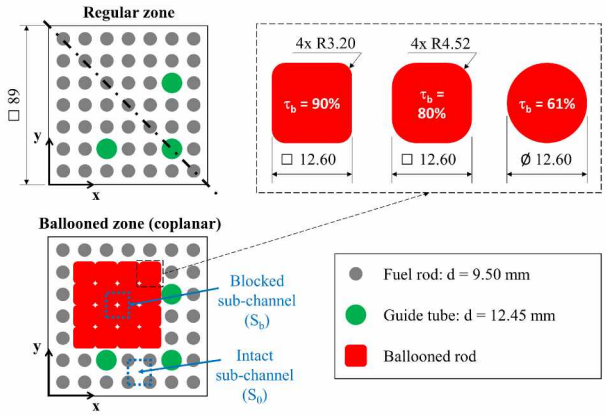

Figure 4: Cross-section of the regular and ballooned zones in coplanar bundles with main dimensions.

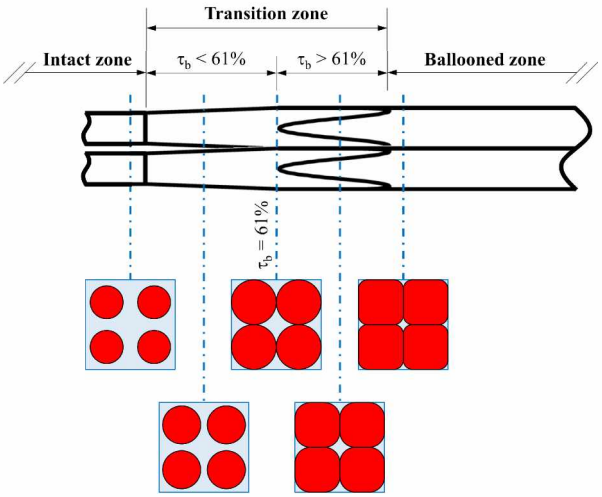

Figure 5: Transition from the intact to the ballooned zone.

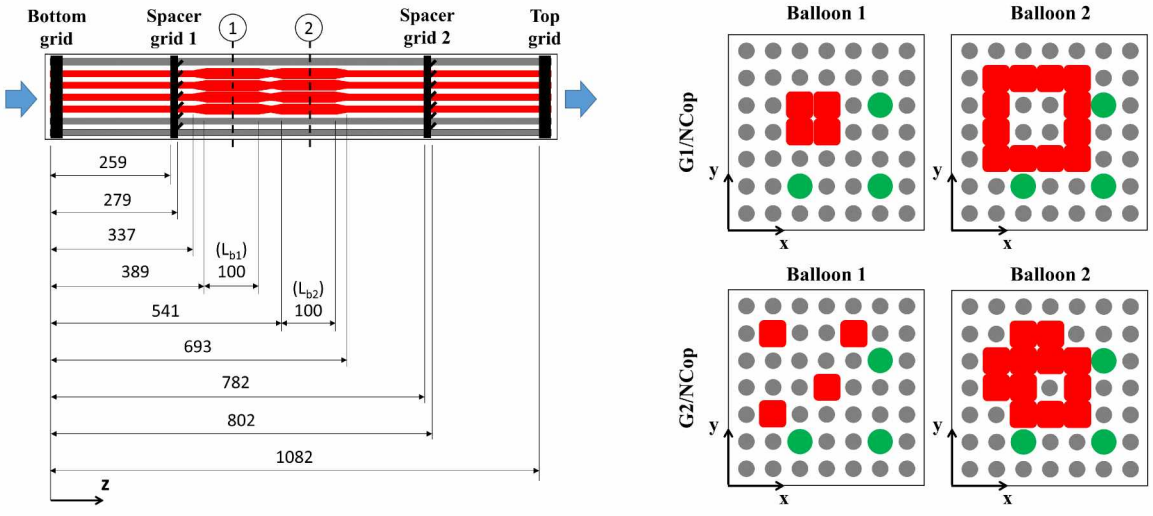

(a) (b)

Figure 6: Non-coplanar bundles: a) axial positions of the grids and the balloons; b) fuel rods arrangement.

G1/NCop, the first four ballooned fuel rods are neighbors and located in the center, creating a blocked sub-channel with 80% blockage ratio that is followed by a barrier of the other twelve ballooned rods. In the second non-coplanar bundle, the first four ballooned fuel rods are sparsely distributed so the sub-channels are not truly blocked, while the other ballooned fuel rods compose the second ballooned zone by completing this 4x4 part according to the first ballooning.

We compare in Fig. 7 the overall blockage ratio for all the tested bundles in this study, which is calculated using Eq. 1 but considering the entire cross-sectional area along the part between the two mixing spacer grids (z' origin is downstream of the first mixing spacer grid). Although some sub-channels are substantially blocked (at least by 61%), the bundle is never blocked by more than 30%. In fact, for the coplanar bundles, the overall blockage ratio varies between 20% and 30%, while for the non-coplanar ones the first and the second balloons result, respectively, in overall blockages of 6.6% and 19.7%.

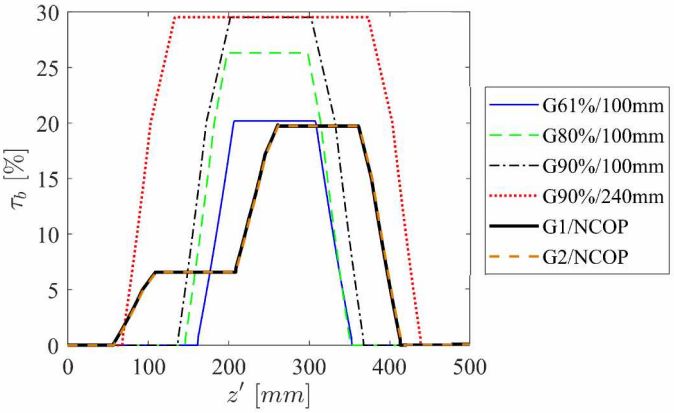

Figure 7: Overall blockage ratio for each bundle between the two mixing spacer grids.

2.3. MRV: sequence, image processing and uncertainties

We performed the MRV experiments using a Bruker Biospec Avance 24/40 mini-imager, which is equipped with a 20 cm gradient coil delivering a 200 mT/m field gradient and with a 16 cm Rapid Biomedical quadrature volume resonator. To encode velocity, we added bipolar gradient pulses to a typical gradient echo pulse sequence [29], as represented in Fig. 8, with the parameters shown in Table 2. The more detailed explanation of the technique and the method used for image processing and uncertainties estimates are available in our previous work [23], so we present herein the main points on these subjects.

Using this MRV sequence, the fluid velocity V in a specific element of volume (usually referred as voxel) is proportional to the signal phase φ:

$$\varphi = \gamma \delta \Delta g V \tag{2}$$

where γ is the gyromagnetic ratio of the nucleus, δ the gradient pulse duration, Δ the time interval between the centers of the two bipolar pulses, and g the gradient intensity. Nevertheless, parameters like the fluid temperature of magnetic field non-homogeneity can affect φ. To mitigate their effects, we acquire two consecutive images using two different gradient intensities (say g_2 and g_1) and take the phase difference between these two images, resulting

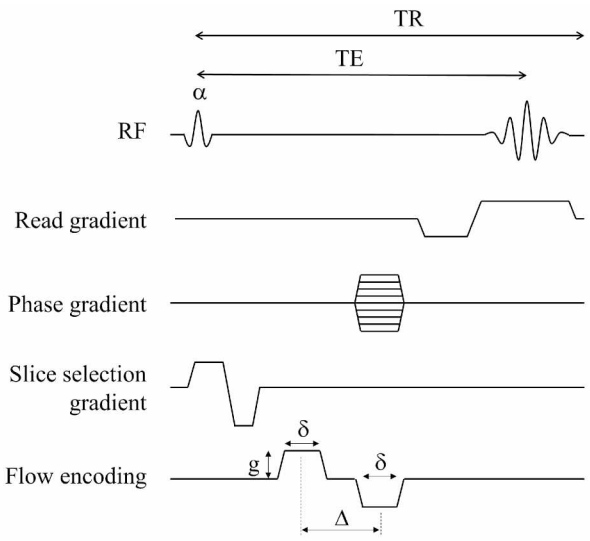

Figure 8: MRV sequence based on the gradient echo method with flow encoding gradients (RF: radiofrequency).

Table 2: Values of MRV parameters used in this study

PARAMETER	**VALUE**
Flip angle (α)	30^{o}
Number of accumulated images	5 – 20
Field-of-view	120 mm
Matrix resolution	256 x 256 pixels
Pixel resolution	0.469 x 0.469 mm^2
Repetition time (TR)	15.0 ms
Echo time (TE)	7.0 ms

in a phase shift image ($\varphi_2 - \varphi_1$) free of side-parametric effects. As a result, the fluid velocity is calculated at a given location by:

$$V = \frac{\varphi_2 - \varphi_1}{\gamma \delta \Delta (g_2 - g_1)} \tag{3}$$

We set $g_1 = 0$ and used fixed values for δ and Δ, which means the only independent variable is the gradient g_2. Its value depends on the fluid velocity field and must be carefully chosen to ensure the measured phase shift is comprised between $-\pi$ and $+\pi$ to avoid phase aliasing. In practice, this choice is done by setting in the MRI software the velocity encoding parameter $VENC$ that represents the maximum measurable velocity without having phase aliasing:

$$VENC = \frac{\pi}{\gamma \delta \Delta g_2} \tag{4}$$

In this study, longitudinal and transverse velocities have very different magnitudes so the $VENC$ was appropriately

set according to the measured velocity component. In general, we used a VENC about 20% higher than the maximum velocity spotted during the experiments.

Having finished the MRV experiments, we could process the data and obtain velocity field images. Nevertheless, using directly the raw data produced very noisy images, like the example shown in Fig. 9a. To overcome this issue, we used masking to remove data of voxels that were not in the water, which provided a cleaner image that was better to visualize (Fig. 9b). Furthermore, masking also allows us to calculate the mean bulk velocity of the flow with the MRV measurements and compare it with the flowmeter acquisitions. Finally, we gathered the three velocity components in only one image by using the color bar to represent the axial velocity intensity (z-direction) and vectors for the transverse velocities (xy-plan), all of them being normalized by the bulk mean velocity ($\widetilde{V}_{z,ref}$, obtained using the flowmeter data) to better compare their magnitudes. To create the transverse velocity vectors, we divided the sub-channels up to four parts, depending on the sub-channel location as shown in Fig. 10. Then, we used the x and y-direction velocity fields to obtain mean values in each part, which resulted in a vector that was placed at the corresponding part's geometrical center. Figure 11 presents an example of the three-component velocity field in a single image with the G90%/100mm bundle.

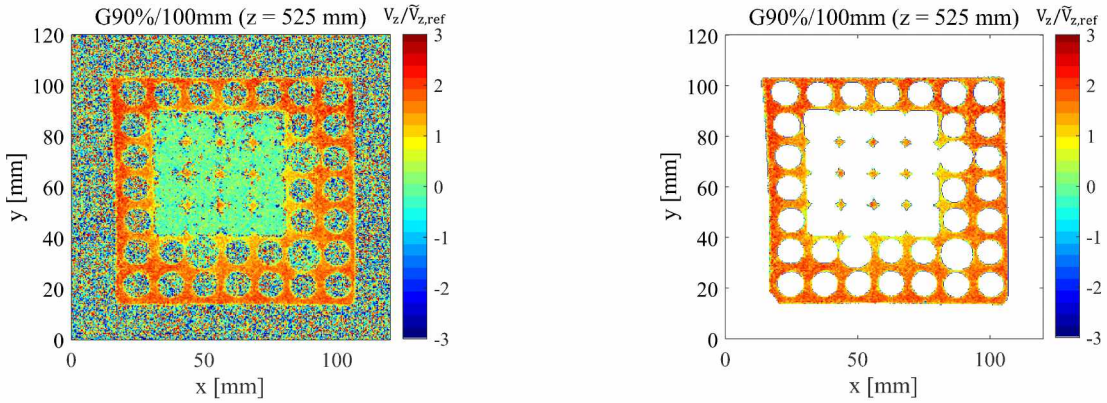

Figure 9: Example of the same normalized velocity field for the G90%/100 mm bundle at 525 mm: a) without masking; b) with masking.

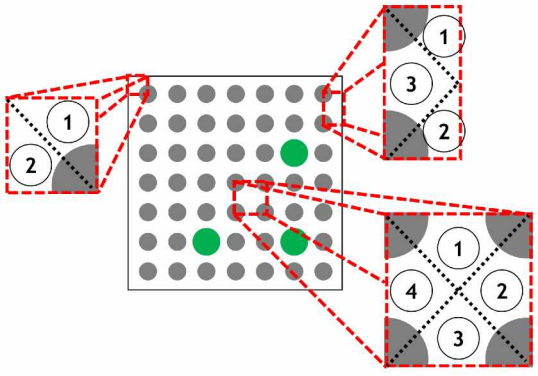

Figure 10: Sub-channel divisions to convert transverse velocity fields into vectors.

To measure the fluid velocity by MRV, some hypotheses are considered, like the static magnetic field inside the scanner is homogeneous and the applied gradients are perfectly linear. Although those are reasonable assumptions,

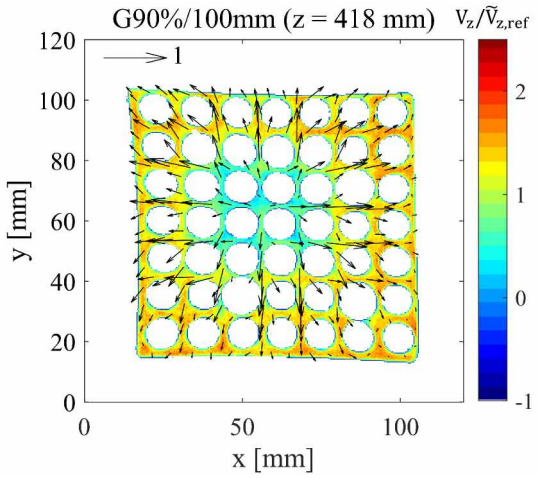

Figure 11: Example of a three-component velocity field image.

they are not entirely true, especially in the presence of metallic materials (like the two aluminum parts on the extremities) and with the use of very high gradients when measuring low velocities. These two undesired conditions induce deterministic errors that can be corrected with preliminary measurements with non-moving water and by normalization of each voxel velocity using the ratio of the flowmeter measurement and the mean bulk velocity obtained by MRV [23]. Having the deterministic errors corrected, we are left only with random errors that serve to estimate the measurement uncertainty. Using the direct uncertainty estimation is not a simple task, as mentioned by Elkins et al. [29], so we used a statistical approach measuring the fluid velocity of a non-moving fluid, which means measuring only the noise. Figure 12 presents the result through a histogram of the measured axial velocities (normalized by the used VENC) for an entire slice and we find a standard deviation of 4.4%, which means the velocity uncertainty in a pixel is about 9% of the VENC with 95% confidence level. As mentioned before, for all the experiments, we set a VENC about 20% higher than the highest velocity found in the measurements. Therefore, the velocity uncertainty in a pixel becomes approximately 20% of the mean bulk velocity. Although this example is for the axial velocity and using one VENC, we found similar uncertainties for all the VENCs we used and for all the velocity components. In the results, we also analyze the mean velocity profile within a blocked sub-channel. Because of this averaging process using dozens or hundreds of pixels, much of the noise is reduced and, consequently, the uncertainty of the sub-channel's mean axial velocity is about 10% of the mean bulk velocity.

2.4. Test procedure

We adopted the following procedure during our experiments once a test section was introduced into the MRI scanner and hydraulic circuit was filled with water. First, we started the pump and adjusted its velocity to provide a 250 lpm flow rate for two minutes minimum, intending to force trapped bubbles to leave the bundle. Afterwards, we purged the air at all the highest points of the hydraulic circuit and stopped the pump so we could place the test section at the first measurement position. Then, we performed signal intensity measurements to ensure the appropriate positioning of the test section and find a capillary tube filled with water to serve as a reference for the slice selection position. Next, the pump rotation velocity was set to supply the highest tested flow rate (in this study, about 245 lpm) and we started acquiring the flowmeter data and performing the MRV for the three velocity

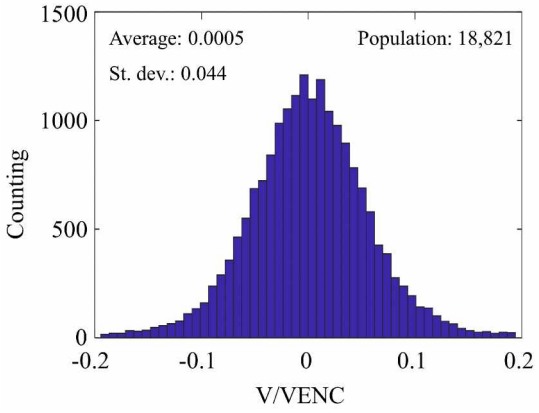

Figure 12: Measurement of MRV noise for the axial velocity using VENC = 50 cm/s.

components at all the selected slices. We repeated these steps for all the tested flow rates, from the highest to the lowest. After, we moved the test section to perform the measurements in the next axial position, proceeding with the aforementioned data and MRV acquisitions. Finally, after testing at all the desired axial positions, the experiment was finished and the data and images were processed as explained in the previous section.

3. Results and discussion

We present the results analyzing each parametric effect starting with geometric characteristics, i.e. blockage ratio, length, and coplanarity, and finishing with the flow rate effect. During the experimental campaign, more than 1,300 velocity fields were measured considering all the tested bundles and flow rates. Generally, the qualitative behavior is the same regardless of the flow rate (as discussed in section 3.5). Therefore, to avoid an excessive and repetitive presentation of the results, we discuss the flow redistribution behavior and the geometric effects using only velocity fields obtained with the lowest flow rate, i.e. about 50 lpm.

3.1. Blockage ratio effect

Figures 13 and 14 present velocity fields at different axial positions for the G61%/100mm, G80%/100mm and G90%/100mm bundles to evaluate the blockage ratio effect on the flow. A schema at the top of the figures indicates where the presented velocity fields are located. Because the three geometries are not exactly the same in the transition zone up- and downstream of the balloon, we compare velocity fields where the ballooning is similar. For example, Fig.13b shows the results in the first transition zone and before the ballooned fuel rods are in contact, which means they are geometrically similar although at different axial positions. Some velocity field images look slightly distorted because of the static field inhomogeneity caused by the presence of metallic parts, as mentioned before. This shape deformation could probably be solved using a spin-echo sequence instead of the gradient-echo used here, or by correcting the image with static magnetic field map. In spite of this undesired deformation, the velocity field measurement was not affected, which ensures the quality of the present results.

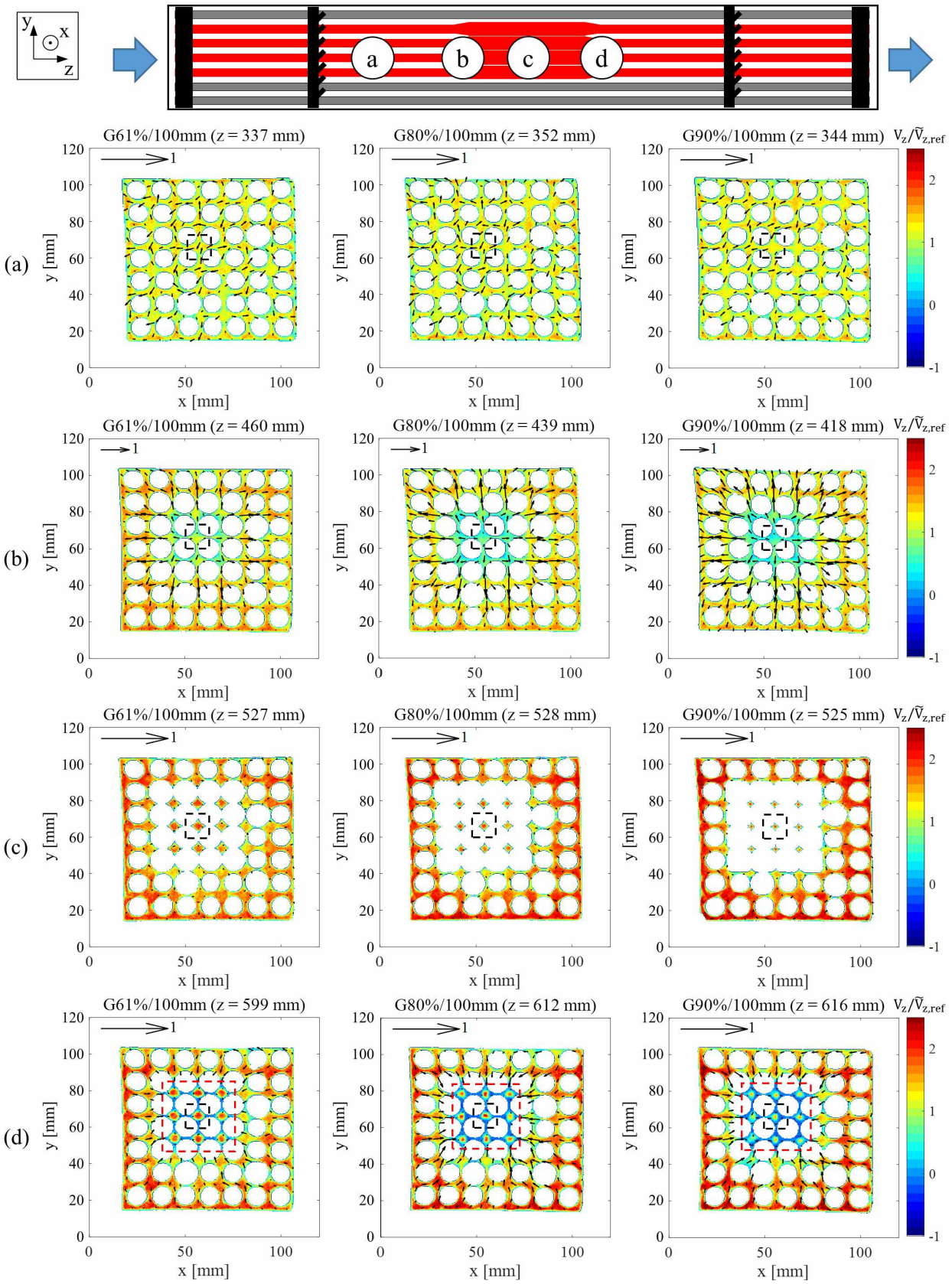

Figure 13: Velocity fields for different bundles comparing the blockage ratio effect - Part I. The sub-channel highlighted by the black box in each bundle was used to trace the profiles in Fig. 16 and to calculate Eq.7. The region highlighted by the red box in (d) is the same presented in Fig. 15.

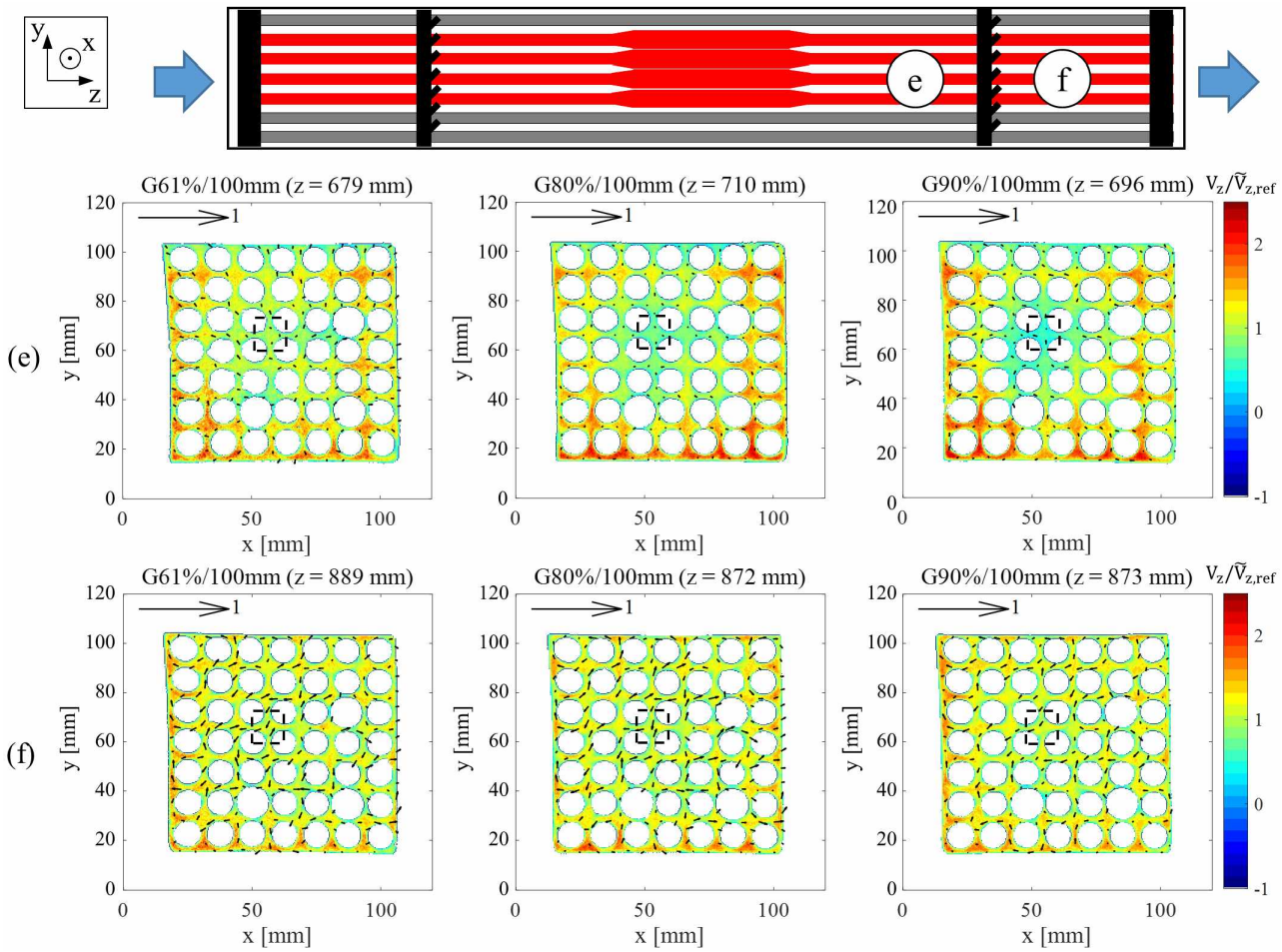

Figure 14: Velocity fields for different bundles comparing the blockage ratio effect - Part II. The sub-channel highlighted by the black box in each bundle was used to trace the profiles in Fig. 16 and to calculate Eq.7.

The fluid flow is nearly homogeneous for all the bundles after passing through the first mixing grid (Fig. 13a), with the presence of relatively low transverse velocities of the swirl caused by the mixing vanes. In the transition zone upstream of the balloon (Fig 13b), the flow redistribution is visible with the decrease in the axial velocity in blocked sub-channels and the increase in the transverse velocity towards intact sub-channels that are less resistant to the flow. The higher the sub-channels' blockage ratio, the more intense these transverse velocities, reaching the same magnitude of the axial velocity. We also notice that the axial velocity in these sub-channels is drastically reduced upstream of the balloon for all the bundles ans this reduction is greater for higher blockage ratios. By comparing the velocity field in the middle of the balloon (Fig 13c) and the first transition zone (Fig 13b), we observe an increase in the axial velocity in the blocked sub-channels because of the reduction in the flow passage area. Meanwhile, the increase in the axial velocity in intact sub-channels is visible due to the flow redistribution, and transverse velocities are negligible in the middle of the balloon.

The flow passage area in blocked sub-channels increases in the transition zone downstream of the ballooned zone (Fig 13d), which induces very low or even negative velocities near the walls of ballooned fuel rods. Figure 15 presents the same velocity fields in Fig 13d but with the color bar comprising only the negative values, showing the flow recirculation only occurs around the four central ballooned fuel rods and it is more intense for higher blockage ratios.

Still on the transition zone downstream of the ballooned zone (Fig 13d), transverse velocities appear towards the blocked sub-channels as a compensation to the previously deviated flow from this region. Nevertheless, the magnitude of these transverse velocities is much lower than the observed upstream of the ballooned zone. Further downstream of the balloon (Fig 14e), the ballooned zone effect is less substantial, but we can still observe lower axial velocities in sub-channels that were previously blocked, while transverse velocities are virtually non-existent. Finally, the second mixing spacer grid mitigates the ballooned zone effect by swirling and, hence, homogenizing the flow (Fig 14f).

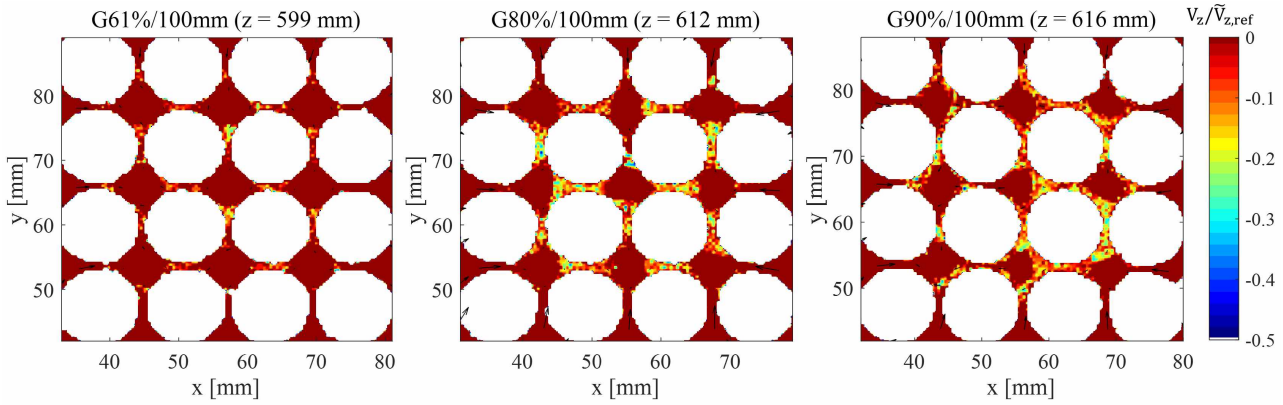

Figure 15: Negative axial velocities observed downstream of the ballooned zones (same region highlighted by the red box in Fig. 13d).

Finally, we also evaluated the blockage ratio effect in Fig. 16 that presents the normalized mean axial velocity profile within the central blocked sub-channel (the one indicated in Fig. 4) along the z-direction. Because the bundles have different lengths, especially in the transitions, the axial positions were normalized with their corresponding zone length (intact, transition and ballooned zones). Furthermore, the normalized velocity $V_{z,n}$ is calculated using the minimum and maximum mean velocities in the central blocked sub-channel among the bundles under comparison ($\widetilde{V}_{z,min}$ and $\widetilde{V}_{z,max}$, respectively) by the following expression:

$$V_{z,n} = \frac{\widetilde{V}_z - \widetilde{V}_{z,min}}{\widetilde{V}_{z,max} - \widetilde{V}_{z,min}} \tag{5}$$

This data processing allows comparing effectively the velocity profiles in this blocked sub-channel regardless of the bundle geometry. We also added background colors for better visualization of the bundle zones and the spacer grids locations.

Figure 16 shows some characteristics already discussed on the velocity field images, like the decrease in the axial velocity in the blocked sub-channel up- and downstream of the balloon and the remarkable homogenization capacity of mixing spacer grids. Nevertheless, more details of the flow in blocked sub-channels are observed. In the first transition zone with the G80%/100mm and G90%/100mm bundles, the decrease in the axial velocity occurs with the flow redistribution and reaches a minimum near the point where ballooned fuel rods touch each other and transverse velocities disappear, followed by a velocity increase due to the reduction in the flow passage area. With the G61%/100mm bundle, the minimum in this zone is very close to the ballooned zone, increasing afterwards because the sub-channel's flow passage area reduces while the flow redistribution is almost impeded due to the very small connection area between blocked sub-channels at this location. The results show explicitly that the higher the blockage ratio, the more intense the velocity reduction upstream of the balloon and the lower the axial velocity within

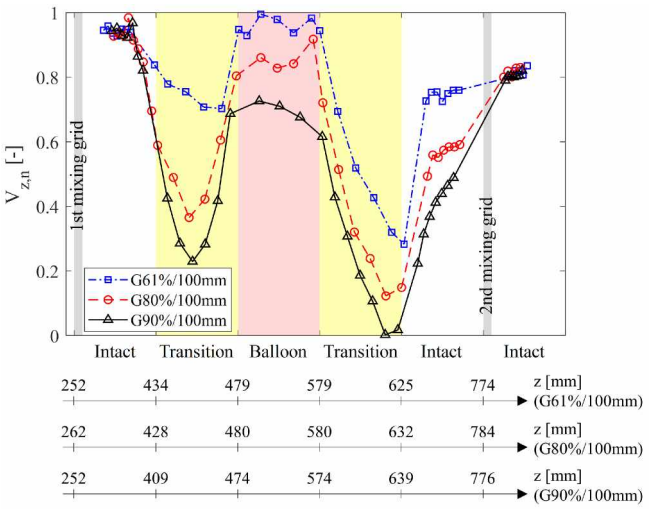

Figure 16: Comparison of the mean axial velocity within the central blocked sub-channel for bundles with different blockage ratios (sub-channels highlighted by a black box in Figs. 13 and 14).

the ballooned zone, although it is nearly the same as in the intact zone upstream with the G61%/100mm bundle. Downstream of the balloon, the flow within the blocked sub-channel is more affected by the flow redistribution for higher blockage ratios, which is consistent with the higher flow recirculation observed in Fig. 15. One common behavior to all bundles is the minimum velocity occurs almost at the end of the transition zone downstream of the balloon, where the sub-channel's flow passage is the largest at this location. The subsequent increase is due to the transverse flow from the intact sub-channels, towards those that were previously blocked, as shown in Fig. 13d.

3.2. Blockage length effect

We present in Fig. 17 velocity fields at four specific positions in the G90%/100mm and G90%/240mm bundles to evaluate the blockage length effect on the flow. The first (Fig. 17a) is located in the first transition zone, the second (Fig. 17b) in the middle of the ballooned zone, the third (Fig. 17c) in the transition downstream of the balloon, and the last (Fig. 17d) after passing through the second mixing spacer grid. Similarly to the blockage ratio comparison, we chose axial positions in both bundles where the ballooning conditions were similar, i.e. the fuel rods deformation were approximately the same. The flow behavior with the G90%/240mm bundle is qualitatively the same as explained previously for the other coplanar bundles. The difference between the two bundles' results is not as evident with the velocity field images as in the precedent section. A better comparison is possible with the graph in Fig. 18 showing the normalized axial velocity evolution in the central blocked sub-channel. This velocity in the ballooned zone with the G90%/240mm bundle is lower than with G90%/100mm because longer blocked sub-channels are more resistant to the flow than shorter ones. For this reason, the minimal axial velocities up- and downstream of the balloon is also more substantial with the G90%/240mm bundle, although the rate of decrease for both bundles is the same.

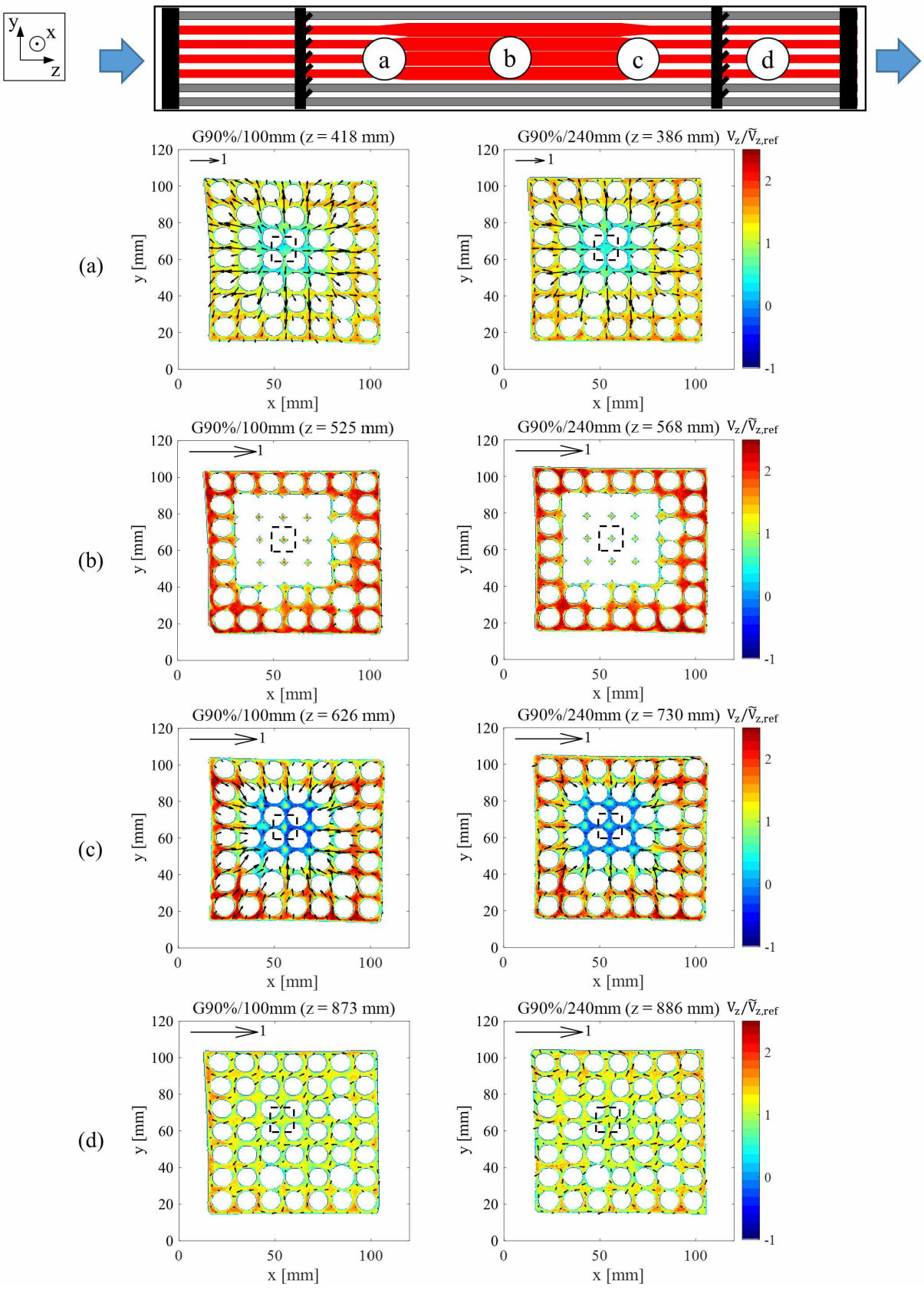

Figure 17: Velocity fields for different bundles comparing the blockage length effect. The sub-channel highlighted by the black box in each bundle was used to trace the profiles in Fig. 18 and to calculate Eq.7.

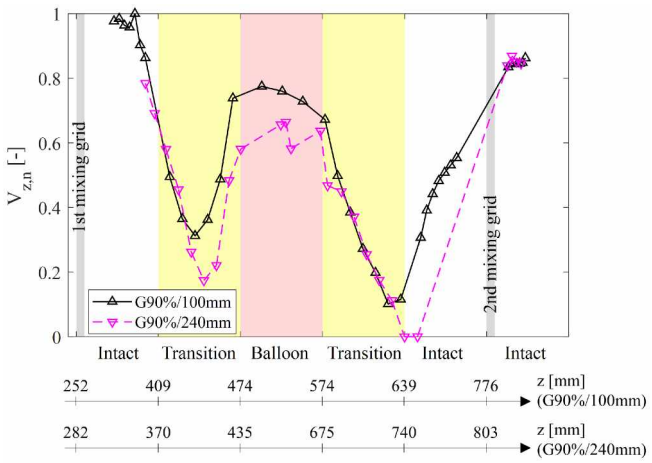

Figure 18: Comparison of the mean axial velocity within the central blocked sub-channel for bundles with different blockage lengths (sub-channels highlighted by a black box in Fig. 17).

One excellent result with the long-ballooned bundle concerning nuclear safety is the great flow homogeneity downstream of the second mixing grid (Fig. 17d) despite the highly heterogeneous velocity field observed right upstream because of the flow redistribution (Fig. 17c). Therefore, considering the mixing spacer grids used in French PWR's, we can affirm that the clad ballooning effect is only restricted to the portion between the two mixing spacer grids where it is located and independently of the ballooned zone blockage ratio or length.

3.3. Blockage coplanarity effect

In this section, we compare the results with the non-coplanar bundles shown in Fig. 6, G1/NCOP being the bundle containing four neighboring ballooned fuel rods in the first ballooned zone, while in the G2/NCOP bundle they are distant from each other. Figure 19a presents the velocity fields for both bundles in the transition zone upstream of the first balloon. For the G1/NCOP bundle, as expected, the flow deviates from the blocked sub-channel in the center. Nevertheless, contrary to the observed with the coplanar bundles, the intensity of these transverse velocities are much lower than the axial velocity. For the G2/NCOP bundle, no significant flow redistribution was observed. These results indicate that the flow redistribution is more intense when there are more neighboring blocked sub-channels, while it is not observable if there is clad ballooning but no sub-channel blocking. In the middle of the first ballooned zone (Figure 19b), the axial velocity field is approximately homogeneous and transverse velocities disappear for both bundles. Then, in the transition zone between the balloons (Figure 19c), the flow redistribution process takes place according to the arrangement of the ballooned fuel rods. With the G1/NCOP bundle, most of the fluid that was in sub-channels neighboring the central blocked one flows towards this sub-channel, while with the G2/NCOP bundle the flow redistributes towards intact sub-channels. In the center of the second balloon (Figure 19d), the flow is once again redistributed with no visible transverse velocity.

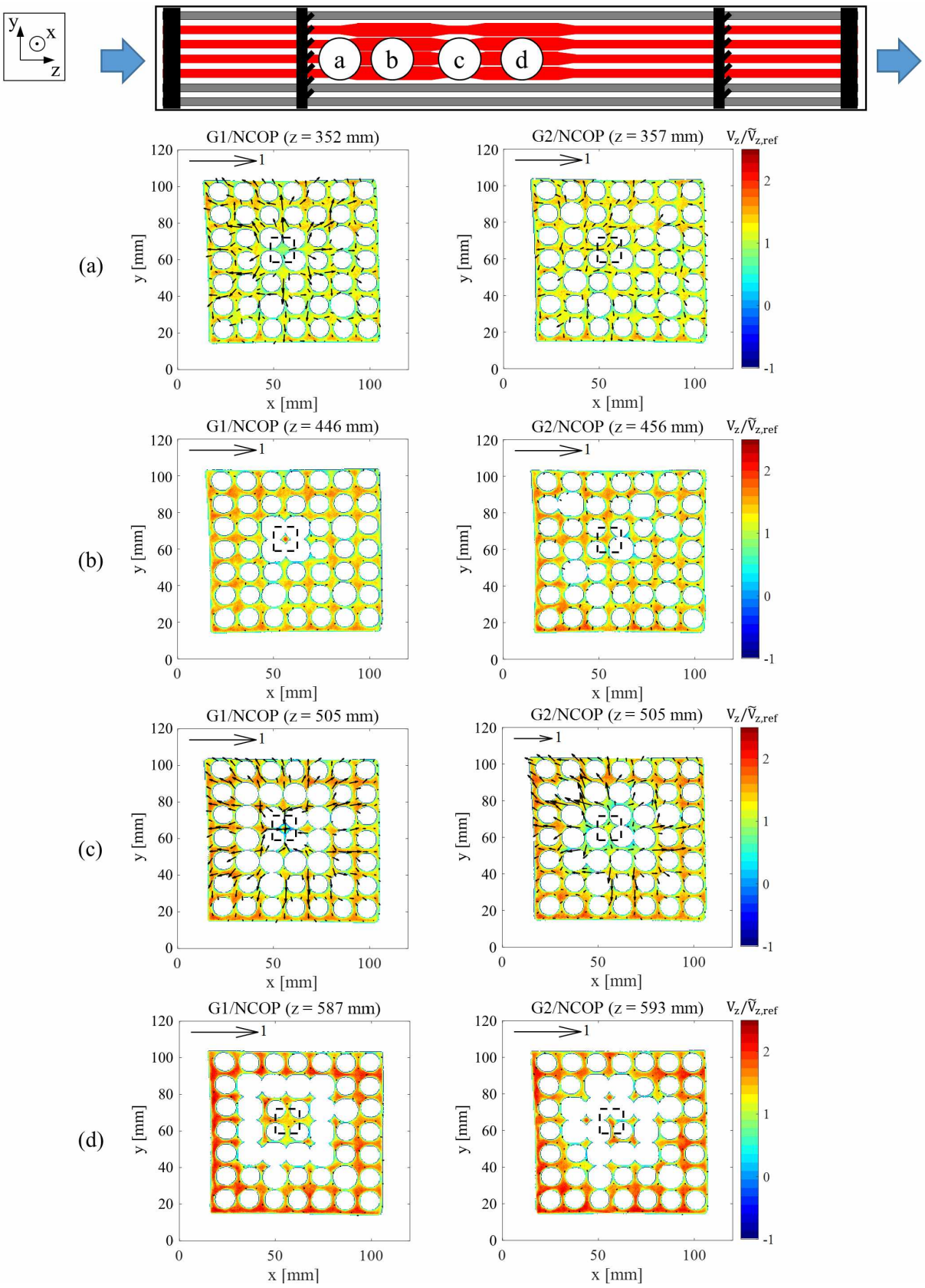

Figure 19: Velocity fields for different bundles comparing the blockage coplanarity effect - Part I. The sub-channel highlighted by the black box in each bundle was used to trace the profiles in Fig. 21.

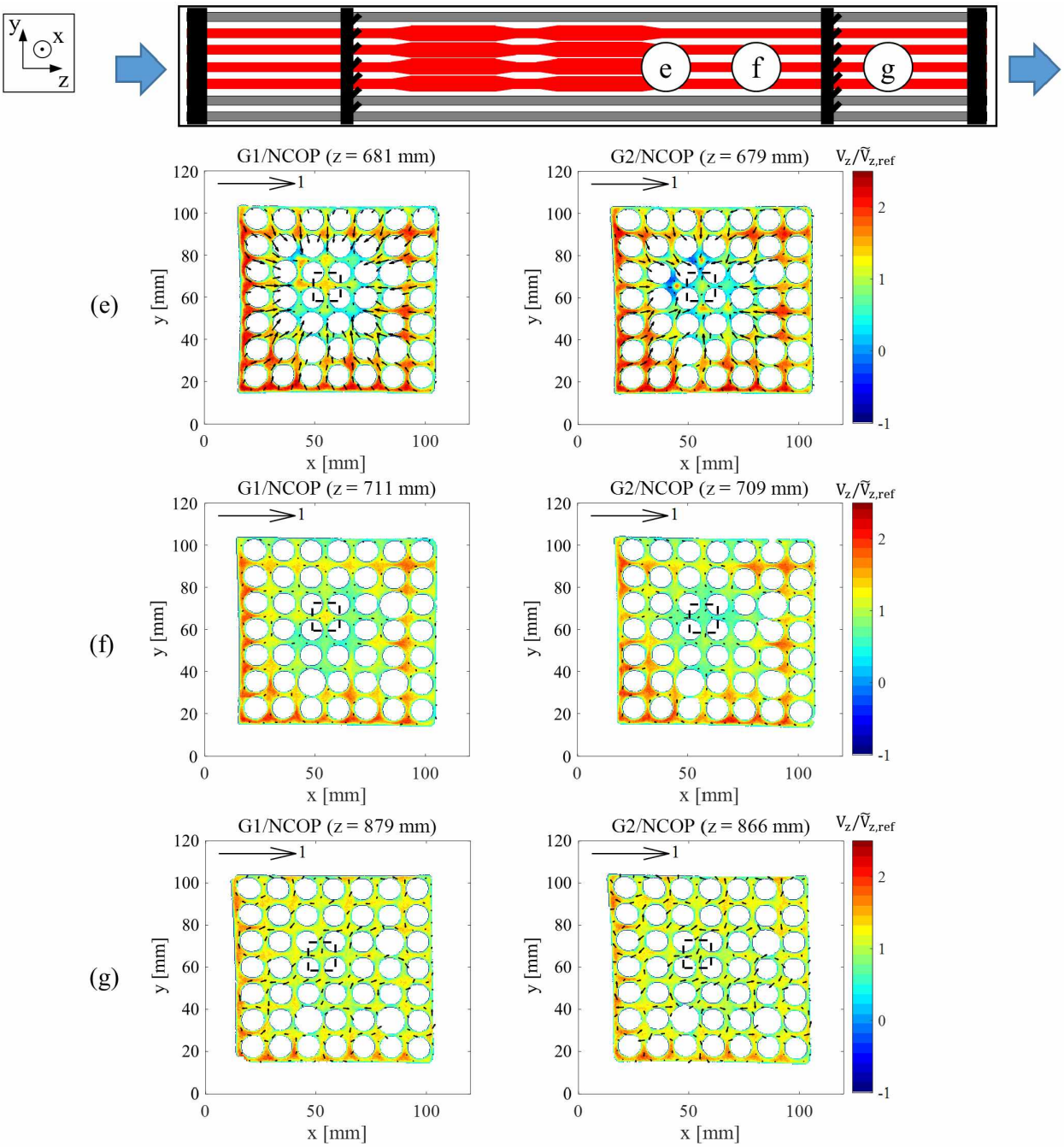

Figure 20: Velocity fields for different bundles comparing the blockage coplanarity effect - Part II. The sub-channel highlighted by the black box in each bundle was used to trace the profiles in Fig. 21.

Downstream of the second ballooned zone (Figure 20e), transverse velocities appear towards the sub-channels that were previously blocked with both bundles, where the axial velocity is lower because of the upstream flow redistribution. However, intense flow recirculation is only observed with the G2/NCOP bundle in the two neighboring sub-channels that were blocked. Still downstream of the second balloon but upstream of the second mixing grid (Figure 20f), the flow is still heterogeneous because of the ballooned zone effect. Although the ballooning arrangement was not the same, the axial velocity magnitude in the affected area at this position is globally very similar for both bundles, although differences are observed if looking individually at each sub-channel. For instance, the axial velocity

is higher in the central sub-channel (previously blocked) with the G1/NCOP bundle than with the G2/NCOP. Finally, as already demonstrated with the coplanar bundles, the fluid is well homogenized after passing through the second mixing spacer grid (Figure 20g).

Figure 21 presents, for each non-coplanar bundle, the change in the mean axial velocity within the central blocked sub-channel, which is highlighted in Fig. 19 and 20 to better localize it in the velocity fields (since it is not as evident to find as in the coplanar bundles). Upstream of the G1/NCOP bundle's first balloon, the velocity decreases, then increases and stays nearly constant in the ballooned zone, similar to the case with the coplanar bundles. Meanwhile, the axial velocity slightly increases in the first transition zone with the G2/NCOP bundle due to the reduction in the sub-channel flow passage area but then decreases in the ballooned zone because the flow slowly deviates towards intact, less-resistant sub-channels. In the transition zone between the balloons, the velocity would sharply decrease with the G1/NCOP bundle as we observed with coplanar bundles. Nevertheless, there is a rapid inflection because the fluid that was in neighboring sub-channels (and that are becoming blocked) flows towards the central sub-channel (as shown in Fig. 19c), resulting in a substantial increase and reaching its highest value in the second ballooned zone. On the other hand, with the G2/NCOP bundle, the central sub-channel's velocity slightly increases in the transition between the balloons and varies little in the second ballooned zone as the fluid exchange with other sub-channels is negligible. In the last transition zone, the sub-channel velocity decreases for both bundles because of the flow passage area expansion, as already observed with coplanar bundles. The flow is eventually homogenized downstream of the second mixing grid, mitigating all the ballooned zone effects.

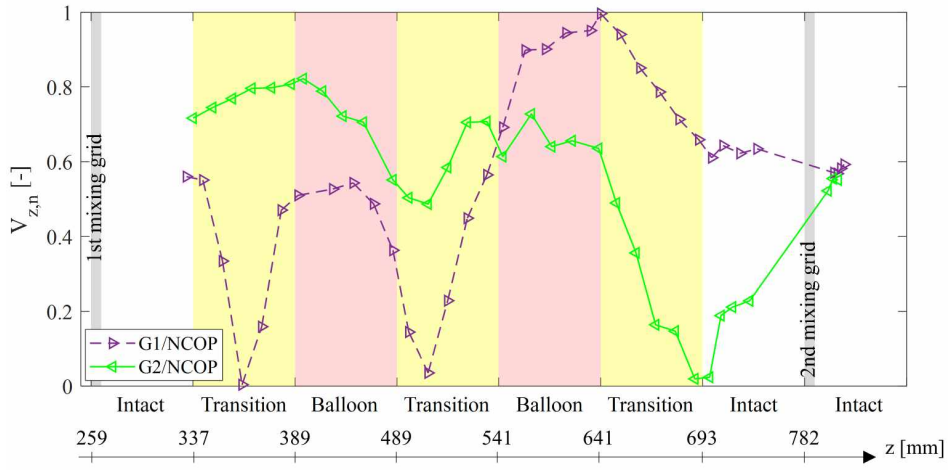

Figure 21: Comparison of the mean axial velocity within the central blocked sub-channel for non-coplanar bundles (sub-channels highlighted by a black box in Figs. 19 and 20).

3.4. Further discussion on the geometric effects

We can deepen the results analysis to establish some characteristics of the clad ballooning effect on the flow redistribution during a LOCA. First, we can estimate the amount of deviated flow R_{dev} with the following expression:

$$R_{dev} = 1 - \frac{\dot{m}_{sc,b}}{\dot{m}_{sc,r}} = 1 - \frac{\rho \widetilde{V}_{z,b} S_b}{\rho \widetilde{V}_{z,0} S_0} \tag{6}$$

$\dot{m}_{sc,b}$ and $\dot{m}_{sc,r}$ being the mass flow rates in a blocked sub-channel in ballooned and regular zones, respectively, ρ the water density (constant), and $\widetilde{V}_{z,b}$ and $\widetilde{V}_{z,0}$ the mean axial velocity in a blocked sub-channel in the ballooned and intact zones, in this order. We obtain the following expression by using Eqs. 1 in Eq. 6:

$$R_{dev} = 1 - \frac{\widetilde{V}_{z,b}}{\widetilde{V}_{z,0}} (1 - \tau_b) \tag{7}$$

We should note that R_{dev} is not a parameter directly related to the flow homogeneity within the ballooned or intact zones, which is discussed in the end of this subsection. Actually, this parameter is useful to understand how much of the fluid still flows within the blocked sub-channel and, consequently, contributes to its cooling by wall-to-steam convection, which is the main heat transfer path in LOCA conditions [9, 10]. The higher the amount of deviated flow, the more critical the cooling of the blocked sub-channel.

Using the experimental results of the central blocked sub-channel (the one highlighted by the black box in Figs. 13), we find that R_{dev} is respectively 59%, 81% and 93% for the bundles G61%/100mm, G80%/100mm and G90%/100mm, which is approximately equal to their corresponding sub-channel blockage ratio. Actually, R_{dev} is slightly higher than the blockage ratio when this last parameter is higher. This happens because the velocity within the blockage sub-channel decreases with the increase in the blockage ratio as demonstrated in Fig. 16. Furthermore, R_{dev} found for the G90%/240mm bundle was 94% (using the sub-channel highlighted by the black box in Figs. 17), which means that the blockage ratio plays a more important role in the amount of deviated flow than the blockage length. Therefore, the blockage ratio is a fine estimate of the amount of redistributed flow, although the velocity within blocked sub-channels is still a little lower for longer balloons (Fig. 18).

Concerning the blockage coplanarity effect, the present results confirmed that coplanar balloons are much more critical than non-coplanar for the fuel assemblies cooling during a LOCA, as already established in past experimental campaigns [5]. Moreover, having separated balloons without really blocking a sub-channel (as in the first ballooned zone with the G2/NCOP bundle) not only is uncritical during a LOCA but also enhances wall-to-steam convective heat transfer with the increase in the flow velocity. These results showed as well two important characteristics of the hydraulics with ballooned zones. First, as the results with the G2/NCOP bundle demonstrated, the clad ballooning becomes indeed an issue in a thermal-hydraulics perspective when there is contact between neighboring clads forming a blocked sub-channel, which leads to substantial reductions in the fluid velocity up- and downstream of the balloons. Second, a downstream ballooned zone can affect the flow redistribution caused by an upstream ballooning and can even change the most critical point to be cooled during the reflooding phase. In general, one of the most critical points is expected to be downstream of a blocked sub-channel because of the flow passage area expansion that decreases the heat dissipation by wall-to-steam convection [5]. In opposition to this reasoning, larger droplets might fall onto the wall downstream of a blocked sub-channel and enhance locally the heat dissipation, as shown by Hishida et al. [30] with a backward-facing step and air-droplets flow. Sub-channel scale studies have shown that wall rewetting can even occur earlier downstream of a ballooned zone because of the same phenomenon [14, 15]. Nevertheless, the results with the G1/NCOP bundle presented the lowest velocity upstream of the first ballooned zone, where droplets could not fall onto the wall, so, for this bundle, this could be the most critical cooling point during a LOCA. This demonstrates the flow redistribution is very specific to the clad ballooning arrangement. More experiments with non-coplanar bundles would be useful to define precisely how the clad ballooning arrangement

affects the flow redistribution.

Finally, we analyzed as well the flow homogeneity along the ballooned bundles, which was evaluated by a homogeneity factor H, proposed in this study and defined by:

$$H(z) = 1 - \frac{\sqrt{\sum_{i=1}^{64} \left[\widetilde{V}_{z,i}(z) - \widetilde{V}_{z,sc}(z)\right]^2 / 64}}{\widetilde{V}_{z,ref}} \tag{8}$$

where $\widetilde{V}_{z,i}$ is the mean axial velocity of the sub-channel i and $\widetilde{V}_{z,sc}$ is the mean axial velocity of all the sixty-four sub-channels in the bundle, both at each axial position z. Therefore, this homogeneity factor is based on the normalized standard deviation of the sub-channels' mean axial velocities. If $H = 1$, we have a perfectly homogeneous flow in the bundle, and the flow heterogeneity increases as H decreases. Following the error propagation analysis described by Moffat [31] and based on the uncertainty of the sub-channels' mean axial velocity, we estimated the mean uncertainty of H was about 0.06 in the intact regions and about 0.15 in the transition and ballooned zones. Thus, Fig. 22a presents the homogeneity factor profiles for the tested coplanar bundles, while Fig. 22b presents the same for the non-coplanar bundles. As a reference, we also added the H values calculated with an intact bundle (G0), that is without balloons, whose results were published in a previous study [23]. In the one hand, for the coplanar bundles, we observe that the flow homogeneity follows the same profile of the central sub-channel's axial velocity. Hence, the locations where the flow is the most heterogeneous are the transition zones, where the transverse velocities are more intense. In the ballooned zone, the flow is a little less homogeneous when the blockage ratio is higher. On the other hand, the flow was almost homogeneous all along the non-coplanar bundles, except downstream of the second ballooned zone. This observation is confirmed as both profiles match exactly the intact bundle's profile until the end of the second balloon. Downstream of this point, for both non-coplanar bundles, we observed a substantial decrease in the axial velocity of previously blocked sub-channels, which may justify the higher flow heterogeneity in the last transition zone. It is interesting to observed that, although the tested non-coplanar bundles had very different configurations and presented very different flow behaviors, especially within the central sub-channel as shown in Fig. 21, their homogeneity factor profiles are practically the same. This is possibly related to the fact that both bundles have the same blockage ratio profile (Fig.7). Therefore, reducing the flow behavior to a single parameter as its homogeneity can hide important information and features, like the minimal axial velocity in the first transition zone observed with the G1/NCOP bundle. Last, the homogeneity factor is virtually the same for all the bundles after the second mixing spacer grid (including the intact bundle), confirming again its remarkable capability to mitigate flow redistribution effects.

As mentioned before, blockages exist in most tube bundle applications, especially in heat exchangers. For example, Tang et al. [32] demonstrated in a numerical study that fouling affects the flow pattern within tube bundles, while da Silva et al. [33] showed experimentally the decrease in the mass flow rate and cooling capacity due to frost accumulation in tube-fin evaporators. Although the results analysis were more focused in PWR applications, the geometric effects on the flow redistribution should be the same, independently of the blockage nature (tube ballooning, deformation, fouling or frost accumulation). Therefore, the present results might also be useful for other research areas beside nuclear engineering.

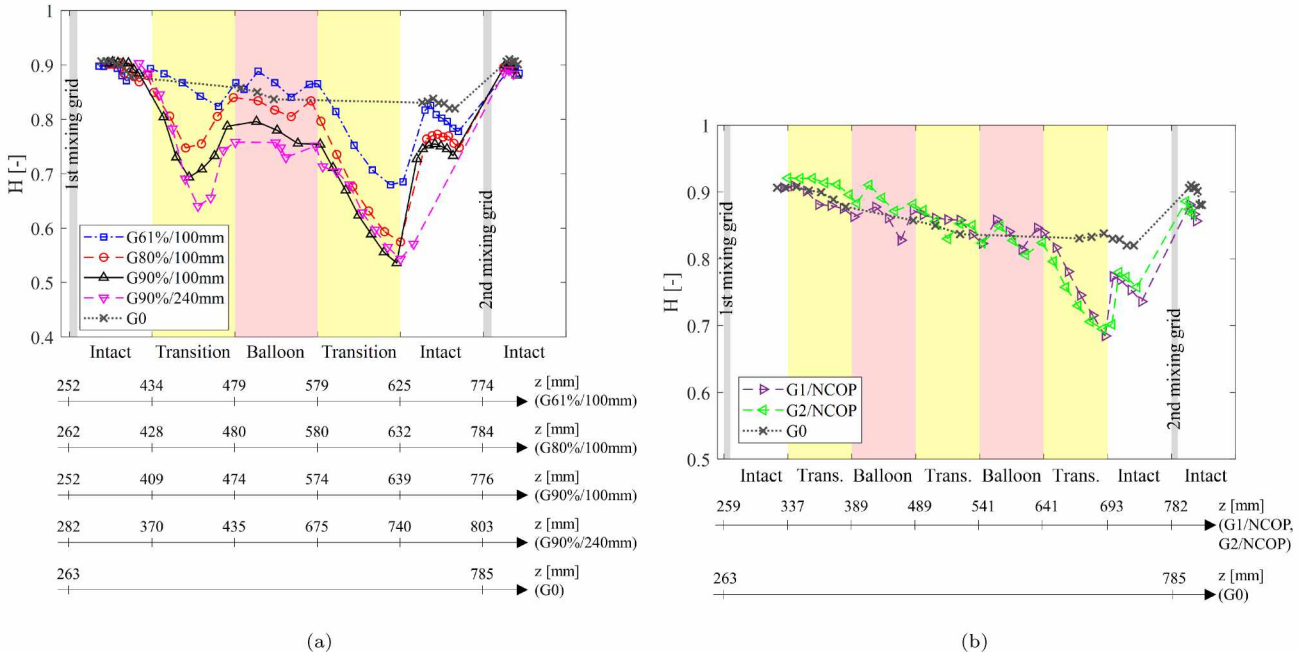

(a) (b)

Figure 22: Flow homogeneity profiles for each tested bundle compared to an intact bundle (G0) [23]: a) coplanar bundles; b) non-coplanar bundles.

3.5. Flow rate effect

As mentioned in the beginning of the results presentation, the flow behavior and redistribution is, in general, qualitatively is the same for all the tested flow rates (approximately 50, 120, 185 and 245 lpm). The only behavioral difference we observed due to the flow rate variation is the velocity field within blocked sub-channels at the transition zone downstream of a ballooned zone, as the example presented in Figure 23 for the four tested flow rates and with the G90%/100mm bundle. For the lowest tested flow rate (Fig.23a), i.e. 50 lpm (which corresponds to a Reynolds number of 1936, considering the bundle's hydraulic diameter and bulk mean velocity), the flow within the blocked sub-channels has a peak at the center, characteristic of a Poiseuille flow profile. As the flow rate increases, and consequently the Reynolds number, the flow profile becomes to flatten, as shown in Fig. 23b for 120 lpm flow rate (Re = 4671). For the two highest flow rates (in Fig. 23c-d for the flow rates of 185 lpm and 245 lpm, whose Reynolds numbers are, respectively, 7223 and 9599), the flow within blocked sub-channels is almost uniform. This behavior occurs because at higher flow rates the flow is turbulent, which increases its momentum diffusivity and, therefore, the fluid is mixed along the flow passage area expansion. For this reason, we did not observe flow recirculation with flow rates other than the lowest as we presented in Fig. 15.

Finally, Fig. 24 presents the velocity profiles within the central blocked sub-channel along the G90%/100mm and G90%/240mm bundles for all the tested flow rates. We chose these two bundles to present the flow rate effect because they are the two cases where the flow redistribution is more significant, as already presented in previous sections. Because we are now comparing different flow rates, the normalized velocity $V_{z,n}$ was again normalized using

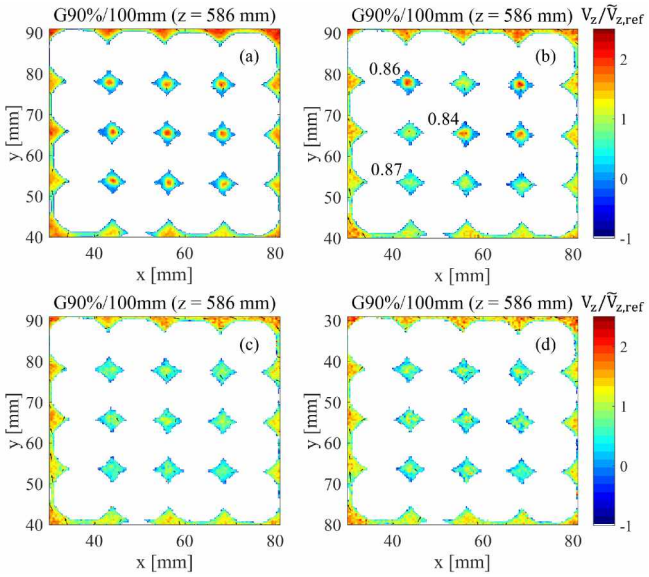

Figure 23: Comparison of the velocity field with the G90%/100mm in the transition zone downstream of the ballooned zone for different flow rates: a) 50 lpm (Re = 1936); b) 120 lpm (Re = 4671); c) 185 lpm (Re = 7223); and d) 245 lpm (Re = 9599). The numbers in (b) are values of $V_{z,n}/V_{z,n,ref}$ calculated with Eq. 9 for sub-channels with different velocity profiles.

the mean bulk velocity according to the following expression:

$$\frac{V_{z,n}}{V_{z,n,ref}} = \frac{\frac{\widetilde{V}_z - \widetilde{V}_{z,min}}{\widetilde{V}_{z,max} - \widetilde{V}_{z,min}}}{\frac{\widetilde{V}_{z,ref} - \widetilde{V}_{z,min}}{\widetilde{V}_{z,max} - \widetilde{V}_{z,min}}} = \frac{\widetilde{V}_z - \widetilde{V}_{z,min}}{\widetilde{V}_{z,ref} - \widetilde{V}_{z,min}} \tag{9}$$

where $V_{z,n,ref}$ is obtained with the use of Eq. 5 with $V_{z,n} = \widetilde{V}_{z,ref}$, which eventually results in a normalization with the difference between the mean bulk velocity and the minimal velocity. These graphs show that the qualitative results are virtually the same for all the tested flow rates. For instance, the minimum velocity is always found at the end of the transition zone downstream of the ballooned zone. Also, the velocity in the ballooned zone is almost the same of the measured in the intact zone upstream of the balloon, although it is slightly lower for lower flow rates. This means that the amount of deviated flow, calculated with Eq. 7, is approximately equal to the blockage ratio regardless of the flow rate. Therefore, we can affirm that the blockage ratio is the predominant parameter on the flow redistribution due to clad ballooning during a LOCA. Nevertheless, a quantitative analysis of the velocity profile show that the decrease in the axial velocity in the transition zone downstream of the balloon is more substantial for higher flow rates. More precisely, the minimum velocity at the end of this transition zone is the same for all the flow rates with the G90%/100mm bundle, while its is slightly higher for higher flow rates with the G90%/240mm bundle. In any case, the flow is always well homogenized after passing through the second mixing spacer grids. Therefore, we can affirm that, when using mixing spacer grids typical of French PWR's, the clad ballooning effect is restricted to the zone between the two mixing spacer grids where the balloon is located regardless of the ballooned zone geometry and for the entire Reynolds number range found during a LOCA (between 1,000 and 10,000).

As shown in Fig. 23, the axial velocity profile in the blocked sub-channels for 120 lpm are different, some similar to a Poiseuille profile and some more flattened, which indicates a transition condition from laminar to turbulent flow. Thus, one may think that the profile presented in Fig. 24 for 120 lpm, which corresponds to the central blocked sub-

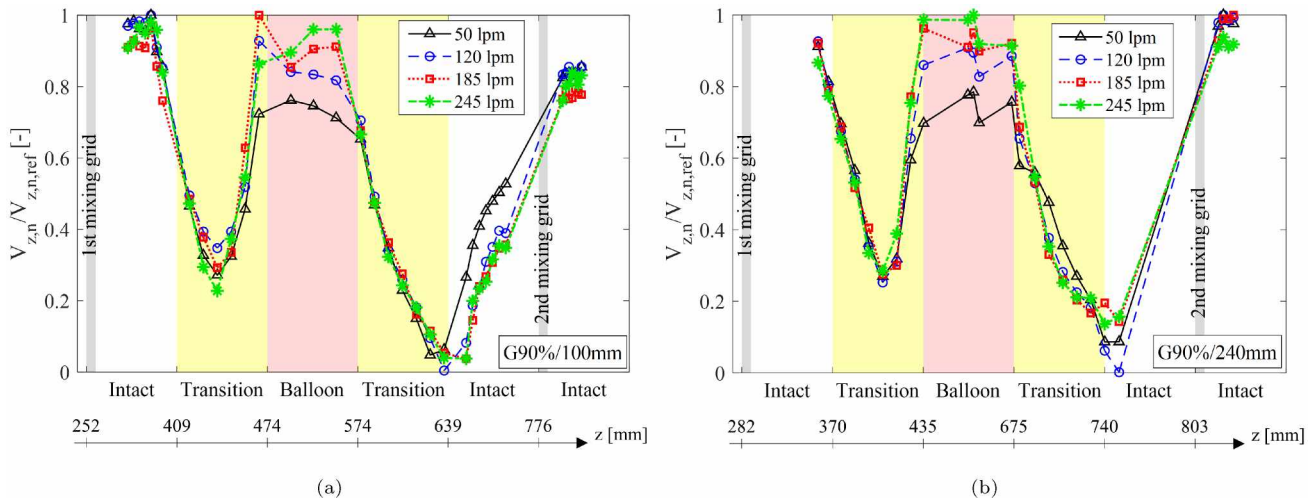

Figure 24: Comparison of the mean axial velocity within the central blocked sub-channel with the G90%/100mm and G90%/240mm bundles for different flow rates (sub-channels highlighted by a black box in Fig. 17).

channel, may vary depending on the sub-channel chosen for the plot. However, this is not the case in the ballooned zone. In Fig. 23, we presented values of $V_{z,n}/V_{z,n,ref}$ for three sub-channels with very different velocity profiles and we find values very close to the one found for the central sub-channel (around 0.85). This confirms as well that the amount of deviated flow is mainly determined by the sub-channel blockage ratio, independently of which blocked sub-channel is considered.

3.6. Applicability of the present study to LOCA

As mentioned in the introduction, the main motivation of the present study was to represent the flow conditions we would find in a hypothetical LOCA. In LOCA conditions, we would actually have mainly a dispersed steam-droplets flow rather than a single-phase steam flow (when the droplets are completely evaporated). The present experiments using liquid water represented the continuous phase only, i.e. steam, by respecting the Reynolds analogy, therefore droplets effect on the flow were not evaluated. This analogy is certainly more valid for the flow condition farther from the water level, where droplets are partially evaporated and the steam flow is accelerated because of the heating. However, the droplets effect may be significant for the flow condition near the water level, where the steam velocity is lower and droplets are larger and more numerous [6].

We can compare the present results with a two-phase flow numerical simulation performed by Ruyer et al. [8] of a configuration with one blocked sub-channel (61% blockage ratio). They demonstrated that the steam flow deviates from the blocked sub-channel to intact ones and returns after the balloon; however, this return towards the previously blocked sub-channel is apparently less intense than the observed in this experiment. Meanwhile, they demonstrated that the droplets do not return to the previously blocked sub-channel. The present experimental results demonstrated that the transverse velocities downstream of the balloon are much lower than those observed upstream. This may explain Ruyer et al.'s results of droplets deviating upstream of the balloon but not returning to the previously blocked sub-channels downstream of it, contrarily to the steam flow.

To the authors' knowledge, there is no experiment in the literature observing the steam-droplets flow behavior in the presence of blocked sub-channels. This is still a challenge that would bring valuable information regarding

the droplets effect on the flow redistribution. A more complicated task would be including as well thermal effects in the flow, because, during a LOCA, not only mechanical non-equilibrium is present but also thermal non-equilibrium. With that said, despite its limitations, the present experimental results are already a first step to better understand this complex flow behavior and improve the validation of numerical simulations.

4. Conclusions

This study presented magnetic resonance velocimetry (MRV) experimental results of three-component velocity field measurements with six different 7x7 bundles with sixteen ballooned fuel rods to evaluate the blockage ratio, length and coplanarity effects on the flow redistribution. The tests were performed with water at different flow rates and the bundles were almost entirely built with plastic material, except for the spacer grids that were made in Inconel and are structurally similar to those used in French PWR's. The ballooned zone was built by 3D-printing because of its complex geometry. Velocity fields at specific positions and with the lowest tested flow rate were presented, as well as the evolution in the mean axial velocity within the central blocked sub-channel along the bundle.

Three bundles with different sub-channel's blockage ratios (61%, 80% and 90%, named G61%/100mm, G80%/100mm and G90%/100mm, respectively) were tested to evaluate its effect, all with the same blockage length (100 mm) and coplanar balloons. The results showed there is an intense flow deviation upstream of the ballooned zone and the transverse velocity magnitude increases with the increase in the blockage ratio, reaching, for instance, the same order of the axial velocity with the G90%/100mm bundle. Also, substantial decreases in the axial velocity are observed up- and downstream of the balloon, the first occurring because of the flow redistribution and the second due to the expansion of the sub-channel's flow passage area. Furthermore, flow recirculation or very low velocities near the walls were detected downstream of the blocked sub-channels. This indicates that, during a LOCA, wall-to-steam convective heat transfer is highly degraded in this region, but also that droplets might fall and enhance locally the heat dissipation, as observed in past sub-channel scale experiments. Finally, the amount of deviated flow is approximately equal to the sub-channel's blockage ratio, although the velocity within blocked sub-channels is relatively lower with the increase in the blockage ratio.

The blockage length does not play a major role in the flow redistribution as the blockage ratio, so the amount of deviated flow was approximately the same for the two bundles used in this parametric analysis (G90%/100mm and G90%/240mm, with respective blockage lengths of 100 mm and 240 mm). Nevertheless, the axial velocity within a blocked sub-channel is slightly lower with longer balloons. Regardless of the bundle's blockage ratio and length, the flow was greatly homogenized by the second mixing spacer grid.

Then, the blockage coplanarity effect was evaluated with two bundles (G1/NCOP and G2/NCOP) and the results demonstrated distanced ballooned fuel rods (first balloon in the G2/NCOP bundle) do not reduce locally the fluid velocity as observed with coplanar bundles. More precisely, the effect of ballooned cladding on the hydraulics is only significant when they are in touch and create a blocked sub-channel (like in the G1/NCOP bundle's first balloon). Moreover, a downstream balloon can affect the flow redistribution caused by an upstream ballooned zone, which can lead to considering different critical points during a LOCA in the thermal-hydraulics point-of-view, as observed with the G1/NCOP bundle. The results also showed that transverse velocities due to flow redistribution are more intense when there are more neighboring blocked sub-channels. More experiments with non-coplanar balloons might

be useful to better describe the blockage coplanarity effect on the flow redistribution.

Finally, the flow rate effect was evaluated with the G90%/100mm and G90%/240mm bundles with four different flow rates (about 50, 120, 185 and 245 lpm, which correspond to Reynolds numbers of 1936, 4671, 7223 and 9599, respectively), covering practically the entire Reynolds number range found during a LOCA (from 1,000 to 10,000). The general behavior of the flow redistribution is virtually the same for all the cases, although flow recirculation downstream of the ballooned zone was only observed with the lowest tested flow rate. When analyzing quantitatively the flow rate effect, the results showed that the decrease in the axial velocity in the transition zone downstream of the ballooned zone is more intense with the increase in the flow rate. Moreover, the amount of deviated flow is insensitive to the flow rate, confirming that the blockage ratio is the prominent parameter on the flow redistribution. Lastly, the flow is always remarkably homogenized when passing through the second mixing spacer grids for all the cases. This confirms that, when using mixing spacer grids typical of French PWR's, the clad ballooning effect is restricted to the portion within the two mixing spacer grids where the balloon is located, for any ballooning geometry and for the entire Reynolds number found in LOCA conditions.

5. Acknowledgment

The authors are thankful to the LEMTA's technical group for their remarkable work building MASCARA experimental apparatus, namely: Jean-Yves Morel, Jérémy Bianchin, Sébastien Lejeune and Franck Demeurie in the Mechanical Group; Mathieu Weber, Simon Becker and Jamal Ouhajjou in the Electronics and Instrumentation Lab.

6. Funding

The experiments with coplanar bundles were completed within the framework of RSNR PERFROI Project from a French State aid managed by the French National Research Agency under the program of Investments for the Future carrying the reference n° ANR-11-RSNR-0017, while the experiments with non-coplanar bundles were financed by IRSN.

References

[1] G. Repetto, C. Dominguez, B. Durville, S. Carnemolla, D. Campello, C. Tardif, M. Gradeck, The R&D PERFROI project on thermal mechanical and thermal hydraulics behaviors of a fuel rod assembly during a loss of coolant accident, 16th International Topical Meeting on Nuclear Reactor Thermal Hydraulics (NURETH-16) 1 (2015) 1–14.

[2] Q.-Y. Ren, L.-M. Pan, W.-X. Zhou, S.-J. Du, Z.-C. Li, Phase distribution characteristics of bubbly flow in 5x5 vertical rod bundles with mixing vane spacer grids, Experimental Thermal and Fluid Science 96 (2018) 451 – 459. doi:https://doi.org/10.1016/j.expthermflusci.2018.04.002.

[3] K. Zhang, Y. Hou, W. Tian, Y. Fan, G. Su, S. Qiu, Experimental investigations on single-phase convection and steam-water two-phase flow boiling in a vertical rod bundle, Experimental Thermal and Fluid Science 80 (2017) 147 – 154. doi:https://doi.org/10.1016/j.expthermflusci.2016.08.018.

[4] C. Yan, J. Shen, C. Yan, Q. Tian, G. Yang, Resistance characteristics of air–water two-phase flow in a rolling 3x3 rod bundle, Experimental Thermal and Fluid Science 64 (2015) 175 – 185. doi:https://doi.org/10.1016/j.expthermflusci.2015.01.009.

[5] C. Grandjean, Coolability of blocked regions in a rod bundle after ballooning under LOCA conditions: Main findings from a review of past experimental programmes, Nuclear Engineering and Design 237 (15) (2007) 1872 – 1886, NURETH-11. doi:https://doi.org/10.1016/j.nucengdes.2007.02.022.

[6] Y. Jin, F.-B. Cheung, S. M. Bajorek, K. Tien, C. L. Hoxie, Investigation of the thermal-hydraulic non-equilibrium in a 7x7 rod bundle during reflood, International Journal of Heat and Mass Transfer 127 (2018) 266 – 279. doi:https://doi.org/10.1016/j.ijheatmasstransfer.2018.08.011.

[7] Y. Jin, F. R. Beck, B. R. Lowery, D. J. Miller, F. B. Cheung, S. M. Bajorek, K. Tien, C. L. Hoxie, Experimental study of droplet sizes across a spacer grid location under various reflood conditions, Experimental Thermal and Fluid Science 94 (February 2017) (2018) 246–257. doi:10.1016/j.expthermflusci.2018.02.017.

[8] P. Ruyer, N. Seiler, B. Biton, F. Lelong, F. Secondi, D. Baalbaki, M. Gradeck, Two-phase flow across a partially damaged core during the reflood phase of a LOCA, Nuclear Engineering and Design 264 (2013) 187 – 194, SI:NURETH-14. doi:https://doi.org/10.1016/j.nucengdes.2013.02.026.

[9] A. V. S. Oliveira, J. D. Peña Carrillo, A. Labergue, T. Glantz, M. Gradeck, Mechanistic modeling of the thermal-hydraulics in polydispersed flow film boiling in LOCA conditions, Nuclear Engineering and Design 357 (2020) 110388. doi:https://doi.org/10.1016/j.nucengdes.2019.110388.

[10] Y. Guo, K. Mishima, A non-equilibrium mechanistic heat transfer model for post-dryout dispersed flow regime, Experimental Thermal and Fluid Science 26 (6-7) (2002) 861–869. doi:10.1016/S0894-1777(02)00195-4.

[11] J. Kim, S. Cho, J.-K. Park, Y.-J. Youn, S.-K. Moon, Experimental study to assess effects of ballooning and fuel relocation on the coolability of fuel rod bundle, Nuclear Engineering and Design 332 (2018) 1 – 10. doi:https://doi.org/10.1016/j.nucengdes.2018.03.013.

[12] Z. Hózer, I. Nagy, M. Kunstár, P. Szabó, N. Vér, R. Farkas, I. Trosztel, A. Vimi, Experimental investigation of the coolability of blocked hexagonal bundles, Nuclear Engineering and Design 317 (2017) 51 – 58. doi:https://doi.org/10.1016/j.nucengdes.2017.03.030.

[13] A. V. S. Oliveira, J. D. Peña Carrillo, A. Labergue, T. Glantz, M. Gradeck, Experimental study of dispersed flow film boiling at sub-channel scale in LOCA conditions: Influence of the steam flow rate and residual power, Applied Thermal Engineering 172 (2020) 115143. doi:https://doi.org/10.1016/j.applthermaleng.2020.115143.

[14] J. D. Peña Carrillo, A. V. S. Oliveira, A. Labergue, T. Glantz, M. Gradeck, Experimental thermal hydraulics study of the blockage ratio effect during the cooling of a vertical tube with an internal steam-droplets flow, International Journal of Heat and Mass Transfer 140 (2019) 648 – 659. doi:https://doi.org/10.1016/j.ijheatmasstransfer.2019.06.012.

[15] K. Kim, B. J. Kim, H. S. Choi, S. K. Moon, C. H. Song, Effect of a blockage length on the coolability during reflood in a 2 x 2 rod bundle with a 90% partially blocked region, Nuclear Engineering and Design 312 (2017) 248–255. doi:10.1016/j.nucengdes.2016.08.031.

[16] L. E. Hochreiter, FLECHT-SEASET program. Final report. NUREG/CR-4167. EPRI NP-4112. WCAP-10926. doi:10.2172/6475435.

[17] S.-H. Hong, S. Kang, J. Kim, J.-K. Park, S.-K. Moon, Reflood experiments at elevated pressures using intact and deformed rod bundles to simulate small and medium break loss-of-coolant accidents, Nuclear Engineering and Design 338 (2018) 209 – 217. doi:https://doi.org/10.1016/j.nucengdes.2018.08.017.

[18] M. Sarkar, K. Velusamy, P. Munshi, O. P. Singh, Analysis of flow and heat transfer through a partially blocked fuel subassembly of fast breeder reactor, Progress in Nuclear Energy 118 (2020) 103142. doi:https://doi.org/10.1016/j.pnucene.2019.103142.

[19] A. A. Campagnole dos Santos, M. Childs, T. D. Nguyen, Y. Hassan, Convergence study and uncertainty quantification of average and statistical piv measurements in a matched refractive index 5x5 rod bundle with mixing vane spacer grid, Experimental Thermal and Fluid Science 102 (2019) 215 – 231. doi:https://doi.org/10.1016/j.expthermflusci.2018.11.009.

[20] T. Nguyen, N. Goth, P. Jones, R. Vaghetto, Y. Hassan, Stereoscopic piv measurements of near-wall flow in a tightly packed rod bundle with wire spacers, Experimental Thermal and Fluid Science 92 (2018) 420 – 435. doi:https://doi.org/10.1016/j.expthermflusci.2017.11.009.

[21] C. Fort, C. D. Fu, N. A. Weichselbaum, P. M. Bardet, Refractive index and solubility control of para-cymene solutions for index-matched fluid–structure interaction studies, Experiments in Fluids 56 (2015) 210. doi:https://doi.org/10.1007/s00348-015-2080-x.

[22] M. Piro, F. Wassermann, S. Grundmann, B. Tensuda, S. Kim, M. Christon, M. Berndt, M. Nishimura, C. Tropea, Fluid flow investigations within a 37 element CANDU fuel bundle supported by magnetic resonance velocimetry and computational fluid dynamics, International Journal of Heat and Fluid Flow 66 (2017) 27 – 42. doi:https://doi.org/10.1016/j.ijheatfluidflow.2017.04.010.

[23] A. V. S. Oliveira, D. Stemmelen, S. Leclerc, T. Glantz, A. Labergue, G. Repetto, M. Gradeck, Velocity field and flow redistribution in a ballooned 7x7 fuel bundle measured by magnetic resonance velocimetry, Nuclear Engineering and Design 369 (2020) 110828. doi:https://doi.org/10.1016/j.nucengdes.2020.110828.

[24] G. Repetto, C. Marquié, B. Bruyère, T. Glantz, Core coolability in loss of coolant accident: the COAL experiments, 16th International Topical Meeting on Nuclear Reactor Thermal Hydraulics (NURETH-16) 1 (2015) 24–37.

[25] T. Glantz, T. Taurines, S. Belon, O. D. Luze, G. Guillard, F. Jacq, Draccar: A multi-physics code for computational analysis of multi-rod ballooning, coolability and fuel relocation during LOCA transients. part two: Overview of modeling capabilities for LOCA, Nuclear Engineering and Design 339 (2018) 202 – 214. doi:https://doi.org/10.1016/j.nucengdes.2018.08.031.

[26] T. Glantz, T. Taurines, O. D. Luze, S. Belon, G. Guillard, F. Jacq, Draccar: A multi-physics code for computational analysis of multi-rod ballooning, coolability and fuel relocation during LOCA transients. part one: General modeling description, Nuclear Engineering and Design 339 (2018) 269 – 285. doi:https://doi.org/10.1016/j.nucengdes.2018.06.022.

[27] G. Repetto, T. Glantz, G. Guillard, B. Bruyère, Q. Grando, Core coolability in loss of coolant accident: the COAL experiments investigating the thermal hydraulics of a rod bundle with blocked area during the reflooding, 17th International Topical Meeting on Nuclear Reactor Thermal Hydraulics (NURETH-17) 1 (2017) 359–372.

[28] G. Repetto, B. Bruyère, S. Eymery, T. Glantz, Thermal hydraulics behavior of a rod bundle with partially blocked area during the reflooding phase of the loss of cooling accident, 11th International Topical Meeting on Nuclear Reactor Thermal-Hydraulics, Operation and Safety (NUTHOS-11) 1 (2016) 1.

[29] C. Elkins, M. Markl, A. Iyengar, R. Wicker, J. Eaton, Full-field velocity and temperature measurements using magnetic resonance imaging in turbulent complex internal flows, International Journal of Heat and Fluid Flow 25 (5) (2004) 702 – 710, selected papers from the 4th International Symposium on Turbulence Heat and Mass Transfer. doi:https://doi.org/10.1016/j.ijheatfluidflow.2004.05.017.

[30] K. Hishida, T. Nagayasu, M. Maeda, Augmentation of convective heat transfer by an effective utilization of droplet inertia, International Journal of Heat and Mass Transfer 38 (10) (1995) 1773–1785. doi:10.1016/0017-9310(94)00308-I.

[31] R. J. Moffat, Describing the uncertainties in experimental results, Experimental Thermal and Fluid Science 1 (1) (1988) 3 – 17. doi:http://dx.doi.org/10.1016/0894-1777(88)90043-X.

[32] S.-Z. Tang, M.-J. Li, F.-L. Wang, Z.-B. Liu, Fouling and thermal-hydraulic characteristics of aligned elliptical tube and honeycomb circular tube in flue gas heat exchangers, Fuel 251 (2019) 316 – 327. doi:https://doi.org/10.1016/j.fuel.2019.04.045.

[33] D. L. da Silva, C. J. Hermes, C. Melo, Experimental study of frost accumulation on fan-supplied tube-fin evaporators, Applied Thermal Engineering 31 (6) (2011) 1013 – 1020. doi:https://doi.org/10.1016/j.applthermaleng.2010.11.006.